⌔Early Evolution of the 23–26 September 2012 U.K. Floods: Tropical Storm Nadine and Diabatic Heating due to Cloud Microphysics

Sam Hardy, David M. Schultz, and Geraint Vaughan

Centre for Atmospheric Science, School of Earth, Atmospheric and Environmental Sciences, University of Manchester, Manchester, United Kingdom

ABSTRACT

Major river flooding affected the United Kingdom in late September 2012 as a slow-moving extratropical cyclone brought over 100 mm of rain to a large swath of northern England and north Wales, with local accumulations approaching 200 mm. The cyclone developed on 20–22 September following the interaction between an equatorward-moving potential vorticity (PV) streamer and Tropical Storm Nadine, near the Azores. A plume of tropical moisture was drawn poleward ahead of the PV streamer over a low-level baroclinic zone, allowing deep convection to develop. Convectively driven latent heat release reduced upper-tropospheric PV near the streamer, causing it to fracture and cut off from the reservoir of high PV over the United Kingdom. Simulations using the Weather Research and Forecasting Model with 4-km horizontal grid spacing in which microphysical heating and cooling tendencies are set to zero, alongside calculations of instantaneous diabatic heating rates and PV tendencies along trajectories, reveal that deposition heating contributed strongly to the fracturing of the PV streamer into a discrete anomaly by directly reducing upper-tropospheric PV to the streamer's east. Condensation heating contributed to lower-tropospheric PV generation along the cold front as the cyclone developed, while cooling due to sublimation, evaporation, and melting modified the PV much less strongly. The results of this case study show that the collocation of strong deposition heating with positive absolute vorticity in the upper troposphere can lead to substantial PV modification and a very different cyclone evolution to that when deposition heating is suppressed.

1. Introduction

Major river flooding affected the United Kingdom in late September 2012 as the deepest September cyclone to cross the United Kingdom in over 30 years (Met Office 2012) brought over 150 mm of rain to parts of northern England and north Wales between 23 and 26 September, resulting in widespread travel disruption and damage to homes and businesses. The impact of the event was enhanced by the antecedent conditions, with England and Wales experiencing its wettest summer

(JJA) in 100 years as a succession of rain-bearing depressions tracked much farther south than usual, leading to near-saturated soil conditions in parts of northern England and accentuating the flooding risk (Parry et al. 2013). The cyclone responsible for the floods developed northeast of Tropical Cyclone Nadine in the eastern North Atlantic on 21 September 2012. A plume of tropical moisture (total precipitable water ≥45 mm) to Nadine's east was drawn poleward ahead of an approaching potential vorticity (PV) streamer (e.g., Martius et al. 2008), facilitating the development of deep convection along a lower-tropospheric baroclinic zone. The interaction between Nadine and the PV streamer reduced atmospheric predictability in the eastern North Atlantic, with some operational forecasts

---

⌔ Denotes Open Access content.

Corresponding author address: Sam Hardy, Centre for Atmospheric Science, School of Earth, Atmospheric and Environmental Sciences, University of Manchester, Simon Building, Manchester, M13 9PL, United Kingdom.
E-mail: sam.hardy@manchester.ac.uk

initialized at 0000 UTC 20 September, prior to the PV streamer–Nadine interaction, erroneously predicting Nadine to move eastward and make landfall over Europe rather than turning southwestward as observed (Munsell et al. 2015; Pantillon et al. 2016).

The cyclone's development within a plume of tropical moisture to Nadine's east suggests that latent heat release enhanced its deepening rate. The key impacts of latent heat release on cyclogenesis are best encapsulated using the PV framework (e.g., Hoskins et al. 1985; Brennan et al. 2008), in which cyclogenesis is viewed as the mutual interaction of finite-amplitude upper- and lower-tropospheric anomalies. Most importantly, PV is modified by a gradient in heating along the absolute vorticity vector (e.g., Raymond 1992; Stoelinga 1996), with positive PV tendencies below and negative PV tendencies above the level of maximum heating. Positive PV anomalies below the midtropospheric heating maximum enhance both the strength of the surface cyclone itself (e.g., Davis 1992; Stoelinga 1996) and mesoscale features such as the low-level jet (e.g., Lackmann 2002). Above the latent heating maximum in the upper troposphere, a combination of direct PV reduction and enhanced divergence promotes downstream ridge building (e.g., Davis et al. 1993; Bosart and Lackmann 1995; Grams et al. 2011), and even more fundamentally can contribute to surface cyclogenesis by slowing the eastward movement of the faster-moving upper-tropospheric PV anomaly, thus keeping the anomaly "phase locked" with the surface cyclone (e.g., Stoelinga 1996; Ahmadi-Givi et al. 2004).

The influence of latent heat release on PV modification and cyclogenesis is clear from the aforementioned studies, most of which focused on condensation heating and neglected the impact of other microphysical processes. Indeed, many early numerical model studies used liquid-only parameterization schemes, which neglected ice-phase processes completely (e.g., Danard and Ellenton 1980; Anthes et al. 1983; Chen and Dell'Osso 1987; Kuo and Reed 1988). Numerical studies have since continued to focus on the dynamical impacts of condensation heating despite using more sophisticated microphysical schemes that include ice-phase processes (e.g., Reed et al. 1993a, 1994; Ahmadi-Givi et al. 2004), or have specifically omitted ice-phase processes from their analysis to focus on condensation heating (e.g., Schemm and Wernli 2014). As a result, the dynamical impacts of microphysical processes other than condensation heating on cyclogenesis are less well understood.

Addressing this lack of understanding, recent studies (e.g., Joos and Wernli 2012; Igel and van den Heever 2014; Martínez-Alvarado et al. 2014; Dearden et al. 2016) have shown that deposition heating provides an additional source of strong latent heating within extratropical cyclones. Indeed, both Joos and Wernli (2012), integrating microphysical latent heating and cooling rates along trajectories, and Igel and van den Heever (2014), spatially and temporally averaging heating and cooling rates, found that deposition heating within their respective cyclones was stronger than or equal to condensation heating. However, despite the consensus on the strength of deposition heating within extratropical cyclones, the PV modification associated with this heating is variable. On the one hand, Dearden et al. (2016) demonstrated that mid- to upper-tropospheric deposition heating, occurring in a region of relatively large absolute vorticity near the upper-tropospheric PV anomaly associated with a North Atlantic summer cyclone, contributed to the formation of a diabatic PV tower (Rossa et al. 2000) and reduced the cyclone's central pressure by 9 hPa during its mature phase. On the other hand, Joos and Wernli (2012) and Martínez-Alvarado et al. (2014) calculated much weaker PV modification due to deposition heating along warm conveyor belt (e.g., Carlson 1980) trajectories, where absolute vorticity is generally small, within two cold-season cyclones.

The need to quantify PV modification by deposition heating within extratropical cyclones, and how this diabatically modified PV influences cyclone track and intensity, is motivated by the uncertainty in the parameterization of ice-phase processes, such as deposition heating, with many existing parameterization schemes unable to fully represent the observed spectrum of ice particle sizes and shapes (e.g., Forbes and Clark 2003; Milbrandt and Morrison 2013; Dearden et al. 2014, and references therein). As a result, variables that depend sensitively on particle size and shape, such as particle fall speed and growth rate, are subject to inaccuracies that can feed back onto the vertical distribution of latent heating and cooling within extratropical cyclones and subsequently onto the dynamics of the cyclones themselves (e.g., Dearden et al. 2016). Indeed, Forbes and Clark (2003) demonstrated in a modeling study that the synoptic-scale development of a rapidly deepening winter cyclone was sensitive to changes in the deposition heating rate within the model.

Motivated by the uncertainty in deposition heating parameterization, the purpose of this paper is to calculate PV modification by deposition heating in a region of enhanced absolute vorticity near the center of a North Atlantic cyclone driven strongly by latent heat release, and furthermore to determine whether deposition heating enhanced the cyclone's deepening rate. The question is answered by combining high-resolution model sensitivity simulations with diabatic PV tendency calculations along trajectories. Knowing that deposition heating

contributed only weakly to PV modification in a region of small absolute vorticity in previous extratropical cyclone case studies (Joos and Wernli 2012; Martínez-Alvarado et al. 2014), PV tendencies are instead calculated directly over and immediately east of the upper-level PV streamer, where absolute vorticity is expected to be large, as the streamer fractures into a discrete anomaly. Demonstrating that deposition heating contributes more than condensation heating to upper-tropospheric PV modification in this case builds on the recent study by Dearden et al. (2016) that highlighted the synoptic-scale response of two summer cyclones to the removal of deposition heating.

The remainder of this article is structured as follows. Section 2 contains a synoptic overview of the interaction between Nadine and the equatorward-moving PV streamer that preceded extratropical cyclogenesis to Nadine's northeast on 20–22 September. Sections 3 and 4 introduce the results from a series of convection-permitting simulations using the Advanced Research version of the Weather Research and Forecasting (WRF-ARW, hereafter WRF) Model. A control simulation in section 3 adequately captures the cyclone's development northeast of Nadine on 20–22 September. Additional simulations in section 4 investigate the cyclone's dynamical response to microphysical heating and cooling, with a focus on deposition heating. In section 5, the contribution of deposition heating to changes in PV within the developing cyclone is examined further by calculating diabatic heating rates and PV tendencies both instantaneously and along trajectories. Section 6 concludes this article.

2. Synoptic overview

The synoptic evolution of this event is documented using Global Forecast System (GFS) analyses from the National Centers for Environmental Prediction (NCEP), available at 6-hourly intervals at $0.5° \times 0.5°$ horizontal and 50-hPa vertical grid spacing. These analyses are complemented with 3-hourly Tropical Rainfall Measuring Mission (TRMM) satellite-based rainfall data, and Advanced Scatterometer (ASCAT) observations from the National Oceanic and Atmospheric Administration (NOAA) with 25-km grid spacing.

At 0000 UTC 20 September, Tropical Cyclone Nadine was located over the eastern North Atlantic (near 37°N, 32°W) and was moving toward the east-southeast at $4 \, m \, s^{-1}$ with maximum sustained surface winds near $25 \, m \, s^{-1}$ and deep convection producing moderate rainfall ($20 \, mm \, h^{-1}$) near the cyclone center (TRMM satellite data, not shown). Upstream and poleward of Nadine over the western North Atlantic, a strong anticyclonic Rossby

wave-breaking event (e.g., Martius et al. 2007, 2008) brought an upper-tropospheric trough and associated PV streamer equatorward, with a stratospheric intrusion of high-PV air (10.5 PVU) [1 potential vorticity unit (PVU) = $10^{-6} \, K \, kg^{-1} \, m^2 \, s^{-1}$] on the 320-K isentropic surface northeast of Nadine and a streamer with PV > 2 PVU extending into the center of the tropical cyclone (Figs. 1a,b). As the PV streamer approached Nadine from the north between 1200 UTC 20 September and 0000 UTC 22 September, it elongated (Figs. 1a–c) and eventually fractured into an isolated anomaly (Fig. 1d) on 320 K. The formation of an isolated PV anomaly is also noted on the 315- and 325-K isentropic surfaces (not shown). Immediately east of this PV anomaly, a 1001-hPa surface cyclone developed along the weak baroclinic zone northeast of Nadine by 0000 UTC 22 September (Fig. 1d). The cyclone moved northeast along the baroclinic zone and deepened further to 995 hPa by 1200 UTC 22 September as a plume of tropical moisture with precipitable water $\geq 45 \, mm$ was drawn poleward into the developing warm sector, ahead of the thinning PV streamer (Fig. 1e). As the cyclone strengthened, deep convection developed and quickly increased in coverage along the narrow tongue of enhanced precipitable water. The cyclone continued to slowly deepen as it moved northeast toward the United Kingdom between 1200 UTC 22 September and 0000 UTC 23 September (Fig. 1f).

During the main period of surface development between 0000 and 1200 UTC 22 September, the upstream, upper-tropospheric PV streamer fractured and reduced in size as it moved almost directly over the slower-moving, surface cyclone, with a reduction in peak 320-K PV from 10.5 to 4 PVU by 1200 UTC 22 September (Figs. 1d,e). The reduction in PV above a region of latent heat release, which leads to the fracture of the upper-tropospheric PV streamer in this case, has been widely documented in the literature for previous cases (e.g., Bosart and Lackmann 1995; Dickinson et al. 1997; Plant et al. 2003; Posselt and Martin 2004), and is discussed further in the next section.

3. Control simulation

The cyclone's early development northeast of Nadine on 20–22 September 2012 was investigated in more detail using WRF, version 3.5.1 (Skamarock et al. 2008). Two model domains were set up (Fig. 2a) using one-way nesting, 60 vertical levels (extending to 50 hPa), horizontal grid spacings of 20 and 4 km, and time steps of 100 and 20 s, respectively. The convection-permitting (4 km) inner domain covered Nadine, the poleward transport of tropical moisture to the east of Nadine, and the entire track of the developing cyclone (Fig. 2b). GFS analyses
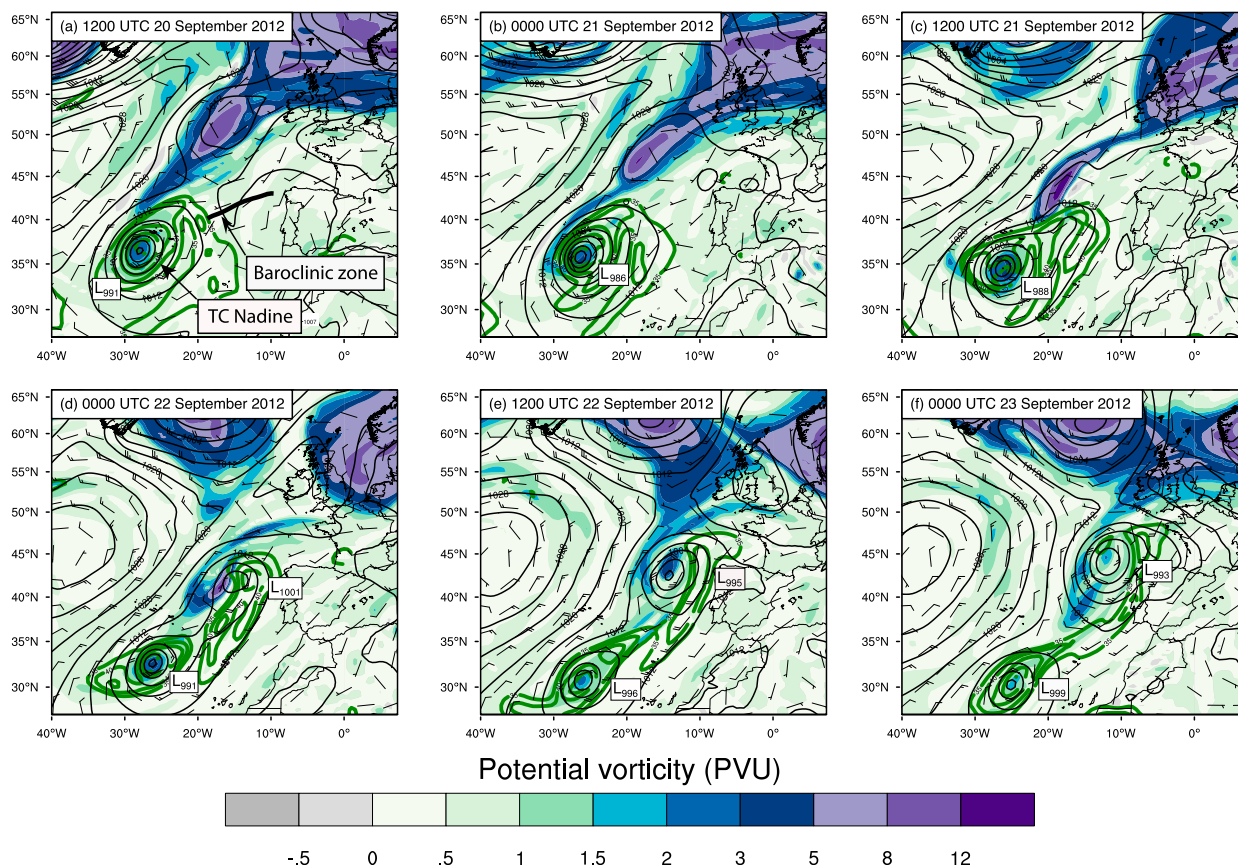
FIG. 1. Potential vorticity (shaded, PVU) on the 320-K isentropic surface, mean sea level pressure (black contours, hPa), total precipitable water (green contours, every 5 mm starting at 40 mm), and horizontal winds averaged over the 700–850-hPa layer (half barb denotes 2.5, full barb denotes 5, pennant denotes 25 m s^{-1}), from Global Forecast System (GFS) 0.5° analysis data: (a) 1200 UTC 20 Sep, (b) 0000 UTC 21 Sep, (c) 1200 UTC 21 Sep, (d) 0000 UTC 22 Sep, (e) 1200 UTC 22 Sep, and (f) 0000 UTC 23 Sep. Tropical Cyclone Nadine and the lower-tropospheric baroclinic zone northeast of Nadine are labeled in (a).

at 0.5° × 0.5° horizontal and 50-hPa vertical grid spacing were used as initial and lateral boundary conditions, with input every 6 h. We used the Yonsei University planetary boundary layer scheme (Hong et al. 2006), the Noah land surface model, and the fifth-generation Pennsylvania State University–National Center for Atmospheric Research Mesoscale Model (MM5) similarity surface layer scheme, based on Monin–Obukhov theory (Monin and Obukhov 1954). The Rapid Radiative Transfer Model for GCMs (RRTMG) scheme (Iacono et al. 2008) was used for both longwave and shortwave radiation. The Kain–Fritsch scheme (Kain and Fritsch 1990) was used on the outer domain, with no cumulus parameterization employed on the inner domain, and the Thompson microphysics scheme (Thompson et al. 2008) was used on both domains. Given the high level of uncertainty associated with the parameterization of ice-phase microphysical processes (e.g., Forbes and Clark 2003; Dearden et al. 2014), the full-physics control simulation (CNTRL) was rerun using the Morrison double-moment

scheme (Morrison et al. 2005), alongside two sensitivity simulations investigating the dynamical response of the cyclone to deposition heating and sublimation cooling, respectively. These results will be discussed in more detail in sections 4 and 5.

The control simulation (CNTRL), initialized at 1200 UTC 20 September, accurately resolved the synoptic-scale evolution of the event, capturing the thinning and fracturing of the PV streamer into an isolated anomaly on 20–21 September and the incipient extratropical cyclone east of the fracturing PV streamer, within the tropical moisture plume, from 1200 UTC 21 September. The thinning and eventual fracturing of the PV streamer was related to several processes. On the synoptic scale, deformation in anticyclonically sheared flow downstream of an upper-tropospheric ridge thinned the streamer as it moved equatorward on 20–21 September (Figs. 3a,b). On the mesoscale, PV nonconservation above a region of 400–650-hPa deposition heating (greater than 1 K h^{-1}) associated with clouds and
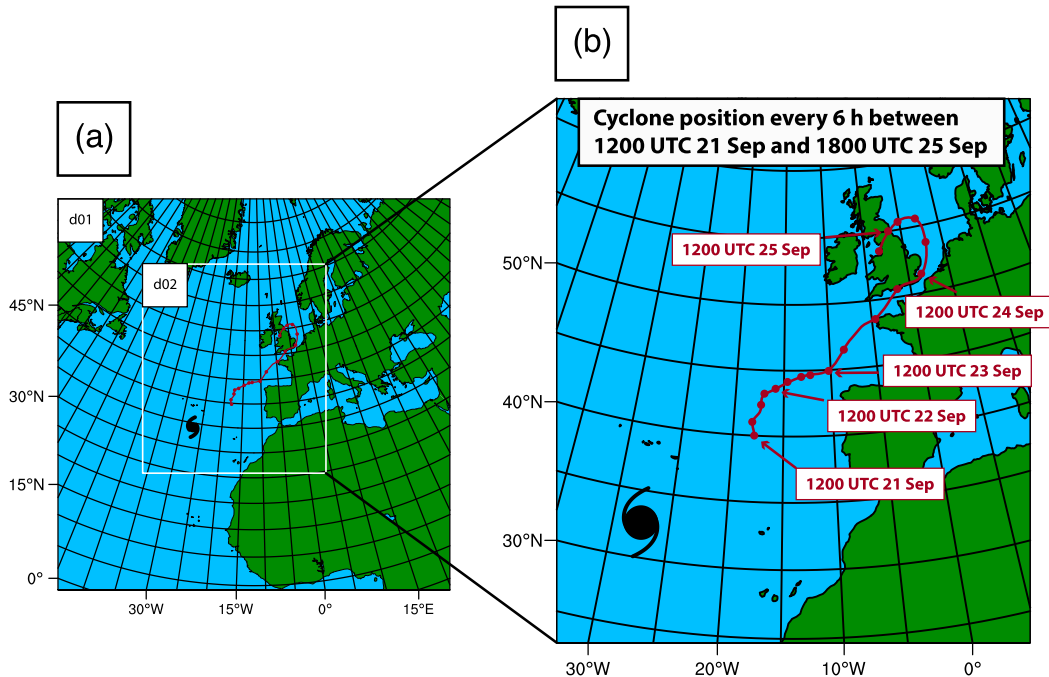
FIG. 2. (a) Location of model domains. The horizontal grid spacing is 20 km on domain 1 (d01) and 4 km on domain 2 (d02). (b) Domain 2, zoomed in. Overlaid are the location of Tropical Cyclone Nadine at 1200 UTC 21 Sep (black TC symbol), and the extratropical cyclone track (red line, with circles denoting the position of the cyclone center every 6 h between 1200 UTC 21 Sep and 1800 UTC 25 Sep) from Met Office analysis.

precipitation to the east of the PV streamer (Fig. 3b) produced negative PV tendencies and reduced upper-tropospheric PV, a process discussed in more detail in section 5. Meanwhile, divergence above this region of deposition heating, and associated with the ascent of the low-PV air, adjacent to the higher-PV air within the PV streamer to the west (refer ahead to Fig. 8a) produced a strengthening horizontal gradient in PV on the streamer's eastern flank (Fig. 3b), in qualitative agreement with GFS analysis data (Figs. 1b,c). Furthermore, this divergence (and associated divergent outflow) slowed the eastward movement of the PV streamer, keeping the streamer coupled to the surface cyclone, as seen in previous case studies of extratropical cyclones driven strongly by latent heat release (e.g., Stoelinga 1996; Plant et al. 2003). The tail of the streamer eventually fractured into an isolated anomaly at 320 K between 1800 UTC 21 September and 0000 UTC 22 September (Fig. 3c) as low-PV air to the east of the PV streamer was advected westward by the aforementioned divergent outflow.

During the period between 1800 UTC 21 September and 0000 UTC 22 September, surface cyclogenesis was likely enhanced by an increase in PV advection over the cyclone center. Previous case studies (e.g., Bosart and Lackmann 1995; Dickinson et al. 1997) have documented how a shortening of the half-wavelength between an upper-level trough and the downstream ridge,

as the ridge builds due to enhanced divergent outflow, steepens the dynamic tropopause and increases upper-tropospheric PV advection over the cyclone center. The shortening half-wavelength in this case is apparent between 1200 UTC 21 September (Fig. 3b) and 0000 UTC 22 September (Fig. 3c) as the PV streamer fractured on 320 K and the ridge built to the northwest of Spain. In addition, radiative cooling also likely contributed to the increasing PV gradient along the dynamical tropopause via the production of positive PV in the lower stratosphere (e.g., Chagnon et al. 2013).

The simulated cyclone showed qualitative similarities with observations, giving us confidence to proceed with sensitivity simulations. First, the simulated cyclone deepened from 999 hPa at 0000 UTC 22 September to 991 hPa at 0600 UTC 22 September (8 hPa in 6 h). This compares favorably both with the analyzed decrease from 1003 hPa at 0000 UTC 22 September to 995 hPa at 0600 UTC 22 September (8 hPa in 6 h), based on Met Office surface charts (Fig. 4), and with the decrease of 6 hPa in 6 h in the GFS 0.5° analysis (Fig. 4). Second, a notable increase in 10-m wind speed accompanied this period of surface development, with a 23 m s^{-1} wind maximum developing west of the low center between 0600 and 1200 UTC 22 September. This wind speed maximum qualitatively agrees with 10-m ASCAT observations, which indicate a concurrent peak of
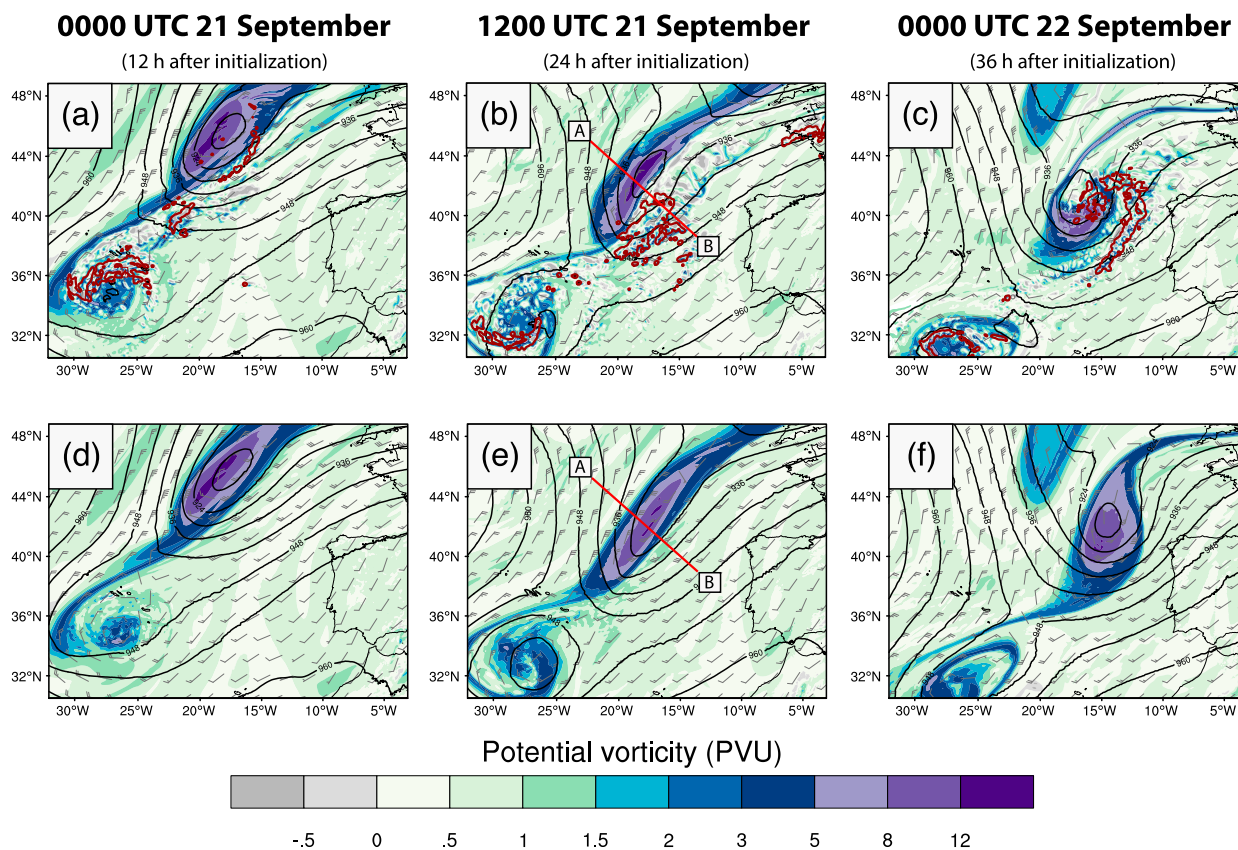
FIG. 3. Potential vorticity (shaded, PVU), and winds (half barb denotes 2.5, full barb denotes 5, pennant denotes 25 m s^{-1}) on the 320-K isentropic surface, 300-hPa geopotential height (black contours, dam), and the deposition heating rate ($\geq$1 K h^{-1}) averaged over the 400–650-hPa layer (dark red contour). Comparison between (top) the control simulation (CNTRL) and (bottom) the simulation with no latent heating (NO_LH) at (a),(d) 0000 UTC 21 Sep; (b),(e) 1200 UTC 21 Sep; and (c),(f) 0000 UTC 22 Sep. The transects A–B in (b) and (e) correspond to the vertical cross-sectional locations in Figs. 7a and 7b, respectively.

21–23 m s^{-1}, although the simulated cyclone is centered about 350 km farther east than indicated by observations (Fig. 5). Third, both the intensity of precipitation along the cold and bent-back warm fronts and the orientation of the two frontal bands at the end of the cyclone's deepening phase at 0600 UTC 22 September exhibit qualitative similarities with TRMM satellite data (Fig. 6). Although the coarser TRMM data (0.25° × 0.25° grid spacing) naturally provide less mesoscale detail than the WRF output, the overall consistency between the WRF accumulated precipitation and the TRMM precipitation rates demonstrates the suitability of the control simulation for the purposes of this study.

4. Sensitivity simulations

The importance of latent heat release to cyclogenesis northeast of Nadine is investigated in a series of WRF sensitivity simulations initialized at 1200 UTC 20 September, summarized in Table 1. Simulations are designed to test the dynamical response of the cyclone to

microphysical heating and cooling. In each simulation, the temperature tendency corresponding to a particular microphysical process in the model's microphysics parameterization scheme (Thompson et al. 2008) is set to zero, analogous to removing the direct and indirect effects of that heating or cooling process. Although such simulations are unphysical, they do provide useful information about the dynamical response of the simulated cyclone to microphysical heating and cooling in the model. Condensation, deposition, and sublimation are discussed in detail. Rainfall evaporation (e.g., Huang and Emanuel 1991) and snow melting (e.g., Szeto and Stewart 1997) were also investigated, but had negligible impact on the cyclone's track and intensity and are thus not described further.

a. No latent heating (NO_LH)

To confirm the expected sensitivity of the cyclone to latent heat release, an experiment (NO_LH) is first designed in which the entire microphysical temperature tendency is set to zero, analogous to running the model
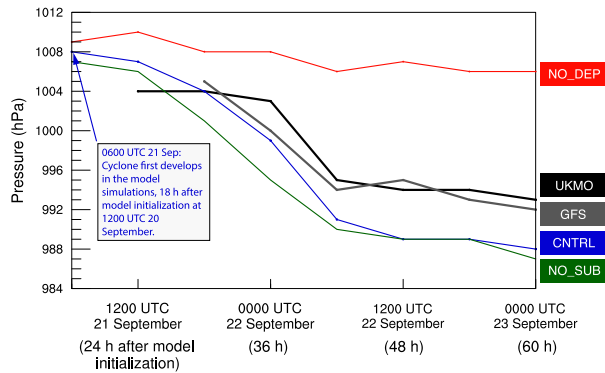
FIG. 4. Time series of mean sea level pressure for the control simulation (CNTRL) and both Met Office (UKMO) and GFS 0.5° (GFS) analysis data, at 6-h intervals between 0600 UTC 21 Sep and 0000 UTC 23 Sep. Also shown are the sensitivity simulations with no deposition heating (NO_DEP) and no sublimation cooling (NO_SUB). All model simulations were initialized at 1200 UTC 20 Sep. In each model simulation, the cyclone appears at 0600 UTC 21 Sep. A cyclone appears 6 h later at 1200 UTC 21 Sep in the Met Office analysis (black line) and 6 h later still at 1800 UTC 21 Sep in the GFS analysis (gray line).

in a "fake dry" configuration (e.g., Reed et al. 1993b). In NO_LH, the equatorward-moving PV streamer initially thinned, as in CNTRL (Figs. 3d,e). In the absence of latent heat release, the development of deep convective precipitation to the east of the PV streamer was limited (Fig. 7), and no surface cyclone developed (not shown). The weaker and less widespread precipitation relative to CNTRL (Fig. 7) had two main impacts. First, direct PV nonconservation above the level of maximum diabatic heating that reduced upper-level PV to the east of the PV streamer in CNTRL did not occur in NO_LH. Second, upper-level divergence was reduced in NO_LH relative to CNTRL (cf. Figs. 8a and 8e). In the absence of these two processes, the PV gradient on the eastern flank of the PV streamer failed to strengthen (cf. Figs. 7a and 7b). Furthermore, the PV streamer moved north-eastward more quickly and downstream ridge building was less pronounced (cf. Figs. 8b and 8f), as documented in several previous case studies on cyclone evolution in the absence of latent heat release (e.g., Davis et al. 1993; Stoelinga 1996; Plant et al. 2003; Ahmadi-Givi et al. 2004).

Nadine weakened rapidly in NO_LH, as expected given the importance of latent heat release to tropical cyclone formation. Consequently, the strength of the tropical moisture plume around Nadine's eastern flank was reduced relative to both CNTRL and the analysis, evidenced by noticeably lower precipitable water and lower-tropospheric θ_e values northeast of Nadine by 0000 UTC 22 September (not shown). To rule out the possibility that the differences between CNTRL and
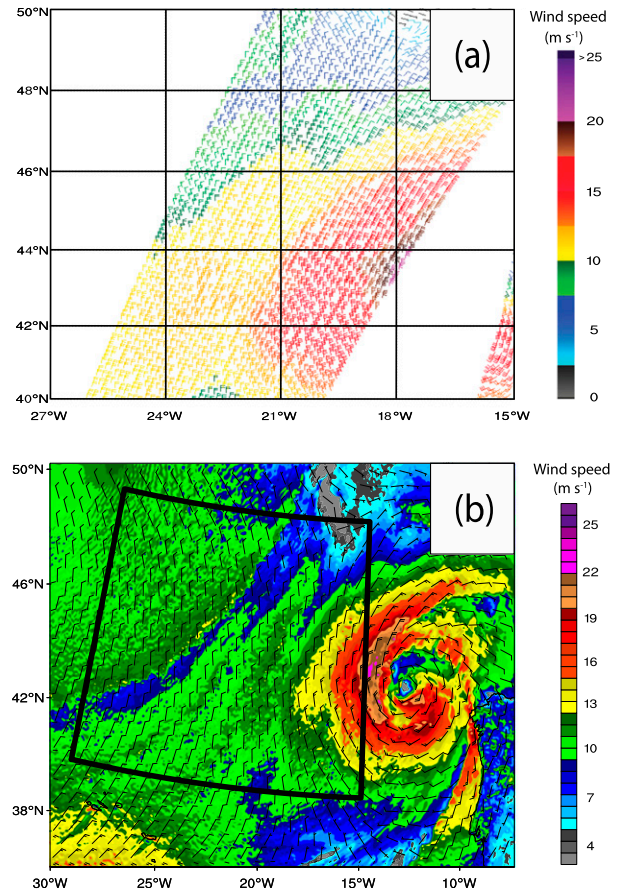
FIG. 5. (a) Advanced Scatterometer (ASCAT) ocean surface wind vector data at 10 m above the ocean surface, from NOAA with 25-km grid spacing and measured by the 1200 UTC 22 Sep 2012 descending pass. Wind barbs (m s^{-1}) are shaded according to the scale. (b) WRF 10-m wind speed (shaded, m s^{-1}) and wind barbs (half barb denotes 2.5, full barb denotes 5, pennant denotes 25 m s^{-1}), valid at 1200 UTC 22 Sep. The black box in (b) corresponds to the area covered in (a). Note that the cyclone in (b) is centered farther east than in (a).

NO_LH were caused by weaker poleward moisture transport related to Nadine's rapid weakening rather than the direct removal of latent heat release, additional simulations were designed. These simulations tested the developing cyclone's sensitivity to the strength of the moisture plume east of Nadine using a similar method to Schumacher et al. (2011). In the initial conditions, the relative humidity (with respect to water) was reduced to 55% at all grid points within the plume with values greater than 55%, decreasing the total precipitable water within the plume from about 40 to 30 mm as the cyclone developed (Fig. 9). The cyclone's deepening rate was only weakly modulated by the strength of the moisture plume, giving us confidence that the differences between CNTRL and NO_LH were related to the direct removal of latent heat release, rather than weaker
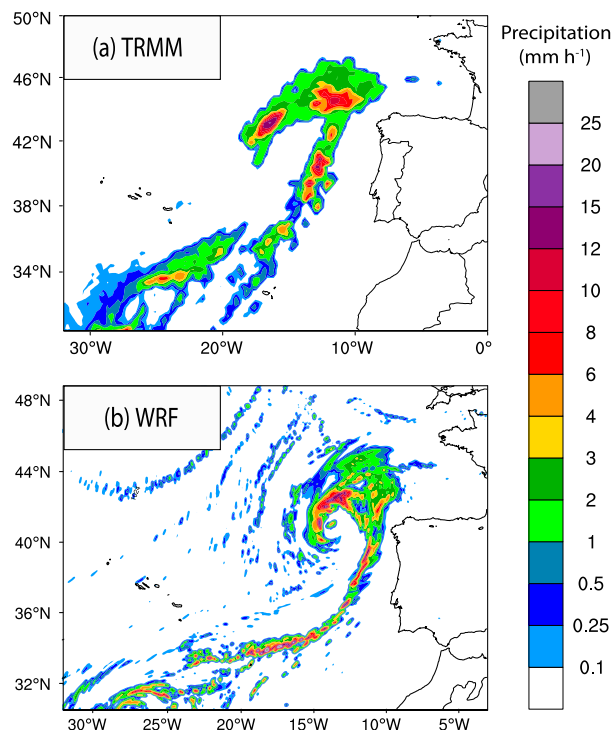
FIG. 6. (a) TRMM satellite-based precipitation rate (mm h^{-1}) at 0600 UTC 22 Sep and (b) hourly accumulated precipitation (mm h^{-1}) from the WRF control simulation for the hour ending 0700 UTC 22 Sep, 43 h after model initialization.

poleward moisture transport associated with Nadine's weakening in NO_LH.

b. No condensation (NO_CON)

No surface cyclone developed in NO_CON, as in NO_LH, suggesting that the direct and indirect effects of condensation heating, in conjunction with the dynamical forcing ahead of the PV streamer, were necessary for cyclogenesis to occur. Despite the similarities between NO_CON and NO_LH, however, subtle differences were observed in the evolution of PV on 320 K (Fig. 10). Although in NO_LH the PV anomaly remained wide (Fig. 10b), in NO_CON a region of lower-PV air (≤ 1.5 PVU) to the north of the positive PV anomaly on 320 K began to encircle the anomaly, reducing its horizontal extent (Fig. 10a). We hypothesize that weak

deposition heating to the north and east of the PV streamer contributed somewhat to a direct reduction in upper-level PV within this region in NO_CON, in contrast to NO_LH in which the diabatic heating rates (and associated diabatic PV tendencies) were zero. However, because average deposition heating rates between 350 and 600 hPa in NO_CON were less than 35% of the heating rates in CNTRL (averaged over the box in Fig. 10a), corresponding diabatic PV tendencies were weak and had little impact on the large-scale evolution of the PV anomaly. The impacts of deposition heating are discussed further in section 4c.

c. No deposition (NO_DEP)

Deposition heating modified the cyclone track and intensity, albeit to a lesser extent than condensation heating. A cyclone developed (unlike in NO_CON) but remained much weaker than in CNTRL: the surface cyclone in NO_DEP was 18 hPa shallower (1007 vs 989 hPa) than in CNTRL after 48 h of the simulation (Fig. 4). Comparison of the 320-K PV evolution at 1800 UTC 21 September and 0600 UTC 22 September (Figs. 11a–d) reveals several differences between NO_DEP and CNTRL that can be attributed to the direct and indirect effects of deposition heating. First, direct PV nonconservation due to deposition heating, hypothesized to be reducing the 320-K PV on the eastern flank of the PV streamer in CNTRL (Figs. 11a,b), did not occur in NO_DEP. The dynamical importance of this PV nonconservation will be discussed in more detail in section 5. Second, upper-level divergence, and associated divergent outflow, in NO_DEP was reduced relative to CNTRL (cf. Figs. 8a and 8c), allowing the PV streamer and associated upper-level trough to move more quickly northeastward by 1800 UTC 21 September in a similar manner to its evolution in NO_LH (cf. Figs. 8b and 8d). This weaker upper-level divergence was directly linked to the underlying smaller and less intense region of precipitation east of the PV streamer in NO_DEP relative to CNTRL (cf. Figs. 12a and 12c).

A similar synoptic-scale response to the removal of deposition heating was seen when rerunning CNTRL and NO_DEP using the Morrison double-moment microphysics scheme (Figs. 13a–d), indicating that the

TABLE 1. Description of WRF control and sensitivity simulations all initialized at 1200 UTC 20 Sep.

Simulation	Description	Cyclone central pressure (hPa) at 1200 UTC 22 Sep
CNTRL	Full-physics control simulation	989
NO_LH	No latent heating from any microphysical processes	—
NO_CON	No condensation heating	—
NO_DEP	No deposition heating	1007
NO_SUB	No sublimation cooling	989
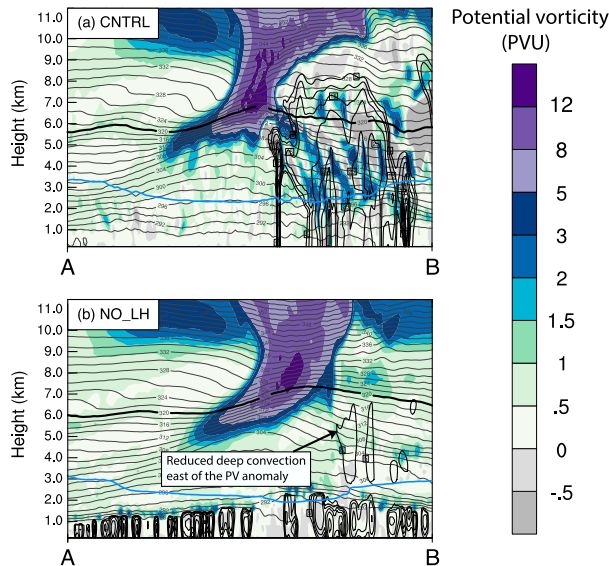
FIG. 7. Vertical cross section of PV (shaded, PVU), potential temperature (thin black contours, K), and simulated reflectivity (thick black contours, every 5 dBZ, starting at 5 dBZ) at 1200 UTC 21 Sep. The freezing level (0°C isotherm) is highlighted in blue, and the 320-K isentrope is highlighted in black. (a) CNTRL and (b) NO_LH. The cross-sectional locations (A–B) in CNTRL and NO_LH correspond to the transects in Figs. 3b and 3e, respectively.

dynamical response of the simulated cyclone was only weakly sensitive to the choice of microphysics scheme. At 0000 UTC 22 September, NO_DEP produced a weaker simulated cyclone than CNTRL with less well-organized precipitation and higher central pressure, for both microphysics schemes (Figs. 13a–d). As a caveat, by the time the cyclone approached the United Kingdom on 23 September, the NO_DEP simulation using the Morrison scheme looked much more like CNTRL than that using the Thompson scheme, an indication that deposition heating reduced the cyclone's central pressure less markedly using the Morrison scheme.

The foregoing discussion suggests that PV nonconservation above the deposition heating maximum reduced upper-level PV to the east of the PV streamer in CNTRL and that this reduction contributed to the fracture of the PV streamer into a discrete anomaly at 320 K. We hypothesize that although PV nonconservation associated with condensation heating reduced PV somewhat on the PV streamer's eastern flank, deposition heating contributed more strongly to this direct reduction in upper-tropospheric PV. This hypothesis will be quantitatively tested in section 5.

d. No sublimation (NO_SUB)

The impacts of sublimation cooling on the evolution of the cyclone are more subtle than for deposition or

condensation heating, in line with previous studies that revealed noticeable mesoscale impacts but little on the cyclone scale (Clough and Franks 1991; Parker and Thorpe 1995; Clough et al. 2000; Forbes and Clark 2003; Forbes and Hogan 2006). Cyclone intensity was slightly increased in NO_SUB relative to CNTRL (Fig. 4), similar to the results of Dearden et al. (2016, see their Fig. 19). However, the difference in cyclone central pressure between the two simulations was generally small (1 hPa or less), except for the period immediately before the cyclone's main development phase (1800 UTC 21 September to 0000 UTC 22 September) when the difference peaked at 4 hPa (Fig. 4). Additionally, the cyclone tracks in the respective simulations were almost identical. A marginally deeper trough developed in CNTRL relative to NO_SUB, but differences in the upper-tropospheric PV were minor both before (cf. Figs. 11a and 11e) and after (cf. Figs. 11b and 11f) the surface cyclone developed. Although the precipitation fields were almost identical in the cyclone's incipient phase in the two simulations (cf. Figs. 12a and 12e), slight differences became apparent in the precipitation field along both the cold front and bent-back front as the cyclone matured (cf. Figs. 12b and 12f), with a more extensive region of heavy precipitation (10 mm h^{-1}) developing along the bent-back front to the north of the low center in NO_SUB. As with NO_DEP, similar results in NO_SUB were obtained when an additional simulation was run with the Morrison double-moment microphysics scheme (cf. Figs. 13e and 13f), indicating that the dynamical response of the cyclone to the removal of sublimation cooling was robust and not a function of the characteristics of either parameterization scheme.

The reduced impact of sublimation cooling on the evolution of the cyclone may be partially explained by its relationship with absolute vorticity, which determines the rate of PV generation or destruction for a given region of diabatic heating or cooling. Over the cyclone as a whole, sublimation cooling was strongest along the cold front, but unlike condensation heating, which occurred between 900 and 750 hPa in a region of large absolute vorticity, the 600-hPa sublimation cooling minimum was unable to modify the PV in the same way because the absolute vorticity was locally small. In a cold-season cyclone with a lower freezing level, and consequently stronger sublimation cooling closer to the enhanced absolute vorticity along the surface front, the impact of sublimation cooling on the mesoscale structure within the cyclone would likely be greater, as documented in the rapidly deepening winter cyclone studied by Clough et al. (2000) and Forbes and Clark (2003). The importance of direct PV modification by

1800 UTC 21 Sep
(30 h after initialization)

0600 UTC 22 Sep
(42 h after initialization)
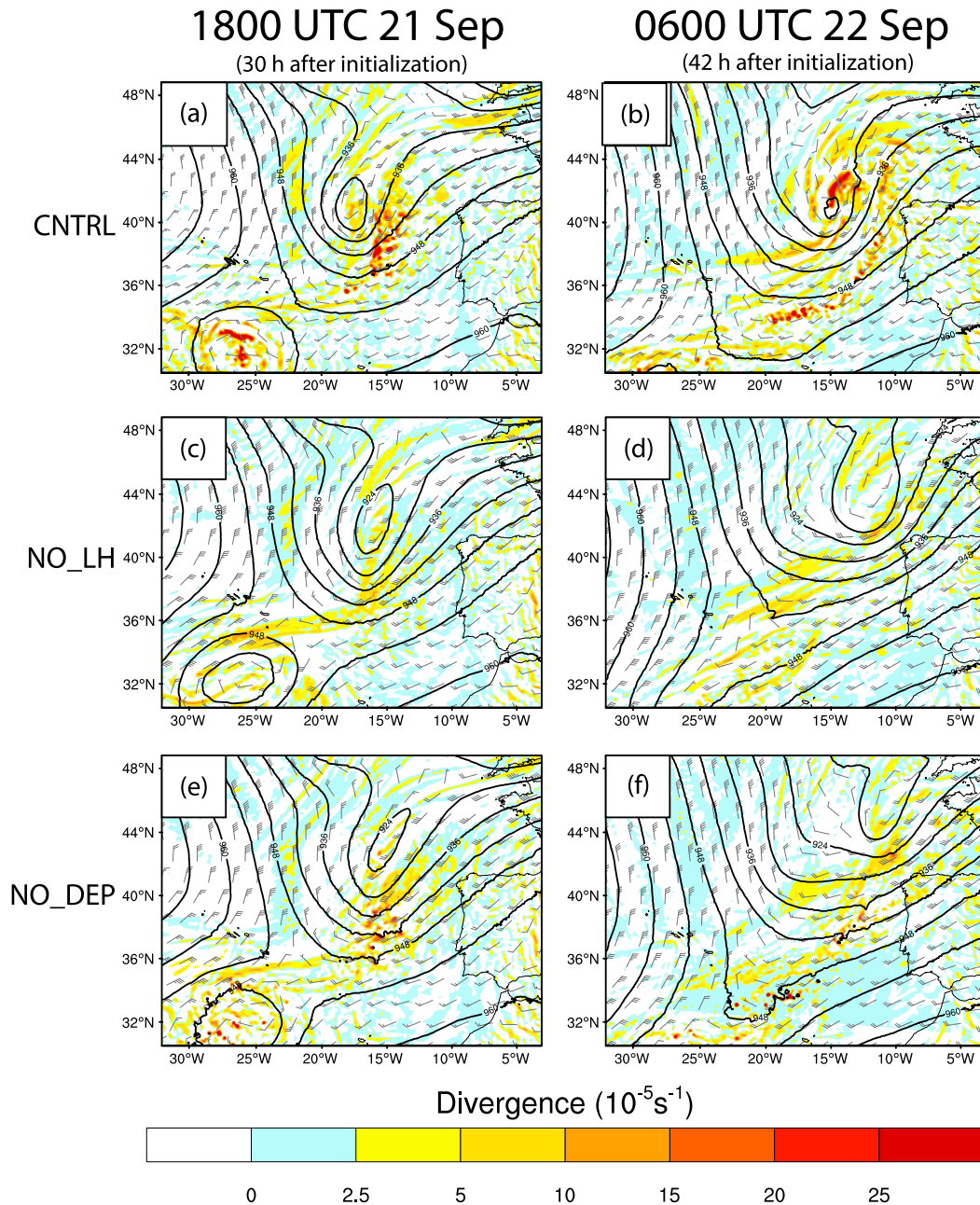
FIG. 8. Divergence (shaded, $10^{-5}\,s^{-1}$), geopotential height (black contours, dam), and winds (half barb denotes 2.5, full barb denotes 5, pennant denotes 25 m s^{-1}), at 300 hPa. Comparison between (top) the control simulation (CNTRL), (middle) the simulation with no latent heating (NO_LH), and (bottom) the simulation with no deposition heating (NO_DEP) at (a),(c),(e) 1800 UTC 21 Sep and (b),(d),(f) 0600 UTC 22 Sep.

diabatic heating and cooling within the cyclone is discussed further in the following section.

5. The importance of diabatic heating to the cyclone's development

Instantaneous heating and cooling rates from 12 microphysical processes are output by the Thompson

scheme: depositional growth of snow, ice, and cloud ice; sublimation of snow, ice, and cloud ice; evaporation of rain; condensation/evaporation of cloud water; melting of snow and graupel; freezing of cloud/rainwater; riming (snow collecting cloud water); graupel collecting cloud water; rimed snow becoming graupel; rain collecting snow; rain collecting cloud ice; and rain collecting graupel. Heating and cooling rates (K h^{-1}) due to

(24 h after initialization) (24 h after initialization)

Precipitable water (mm)

30   32.5   35   37.5   40   42.5   45   47.5   50   52.5   55
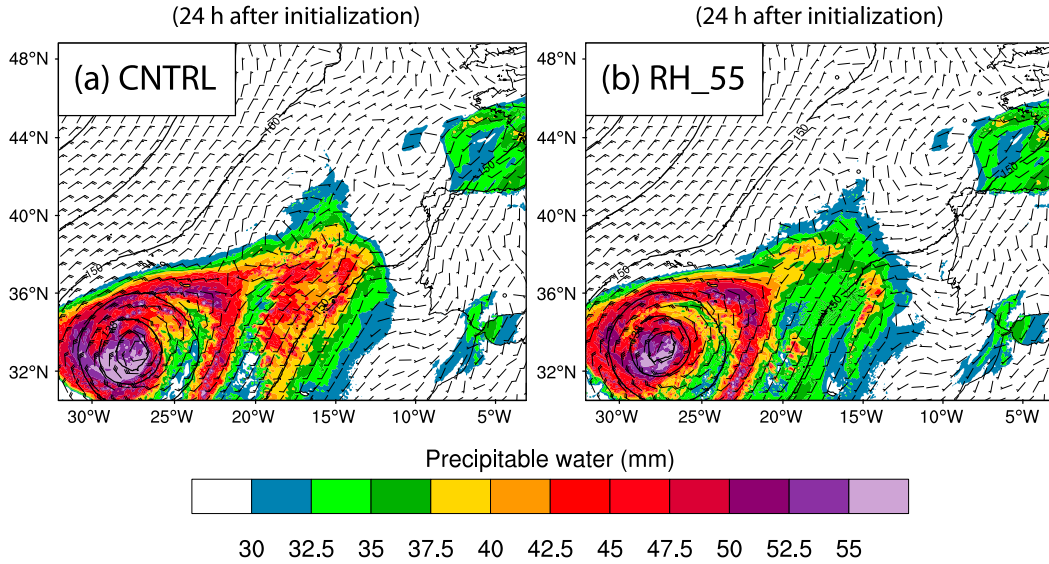
FIG. 9. Total precipitable water (shaded, mm), geopotential height (black contours, dam), and winds (half barb denotes 2.5, full barb denotes 5, pennant denotes $25\,\mathrm{m\,s^{-1}}$), at 850 hPa. Comparison between (a) the control simulation (CNTRL) and (b) the simulation with relative humidity reduced to 55% within the moisture plume east of Nadine (RH_55) at 1200 UTC 21 Sep, 24 h into the two simulations.

deposition, sublimation, evaporation, condensation, melting, and freezing are output separately and analyzed further in this section. The other heating and cooling processes are neglected in the analysis but are included in the total temperature tendency (refer ahead to Fig. 14). These instantaneous heating and cooling rates, output every 10 min from the model, allow for the calculation of PV tendencies within the cyclone using a modified form of the PV tendency equation that neglects friction (Hoskins et al. 1985):

$$\frac{D}{Dt}\mathrm{PV} = \frac{1}{\rho}\boldsymbol{\zeta} \cdot (\nabla\dot{\theta}),\qquad(1)$$

where ρ is the density, $\boldsymbol{\zeta}$ is the absolute vorticity vector, $\nabla\dot{\theta}$ is the gradient of the heating or cooling rate

(42 h after initialization) (42 h after initialization)

Potential vorticity (PVU)

-.5   0   .5   1   1.5   2   3   5   8   12
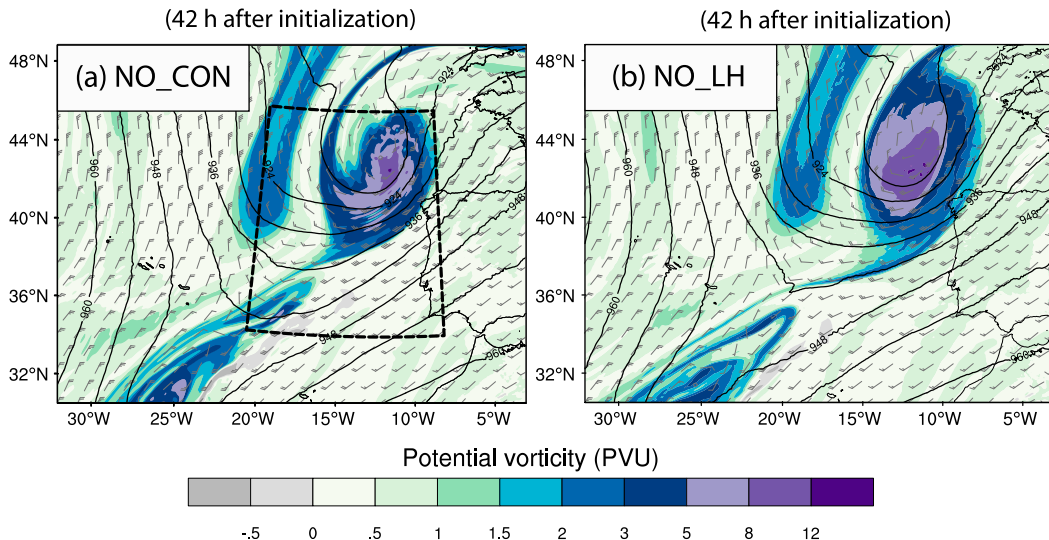
FIG. 10. Potential vorticity (shaded, PVU) and winds (half barb denotes 2.5, full barb denotes 5, pennant denotes $25\,\mathrm{m\,s^{-1}}$), on the 320-K isentropic surface; 300-hPa geopotential height (black contours, dam). Comparison between (a) the simulation with no condensation heating (NO_CON) and (b) the simulation with no latent heating (NO_LH) at 0600 UTC 22 Sep. Overlaid in (a) is the domain for the area-averaged heating rate calculation (thick black dashed lines).
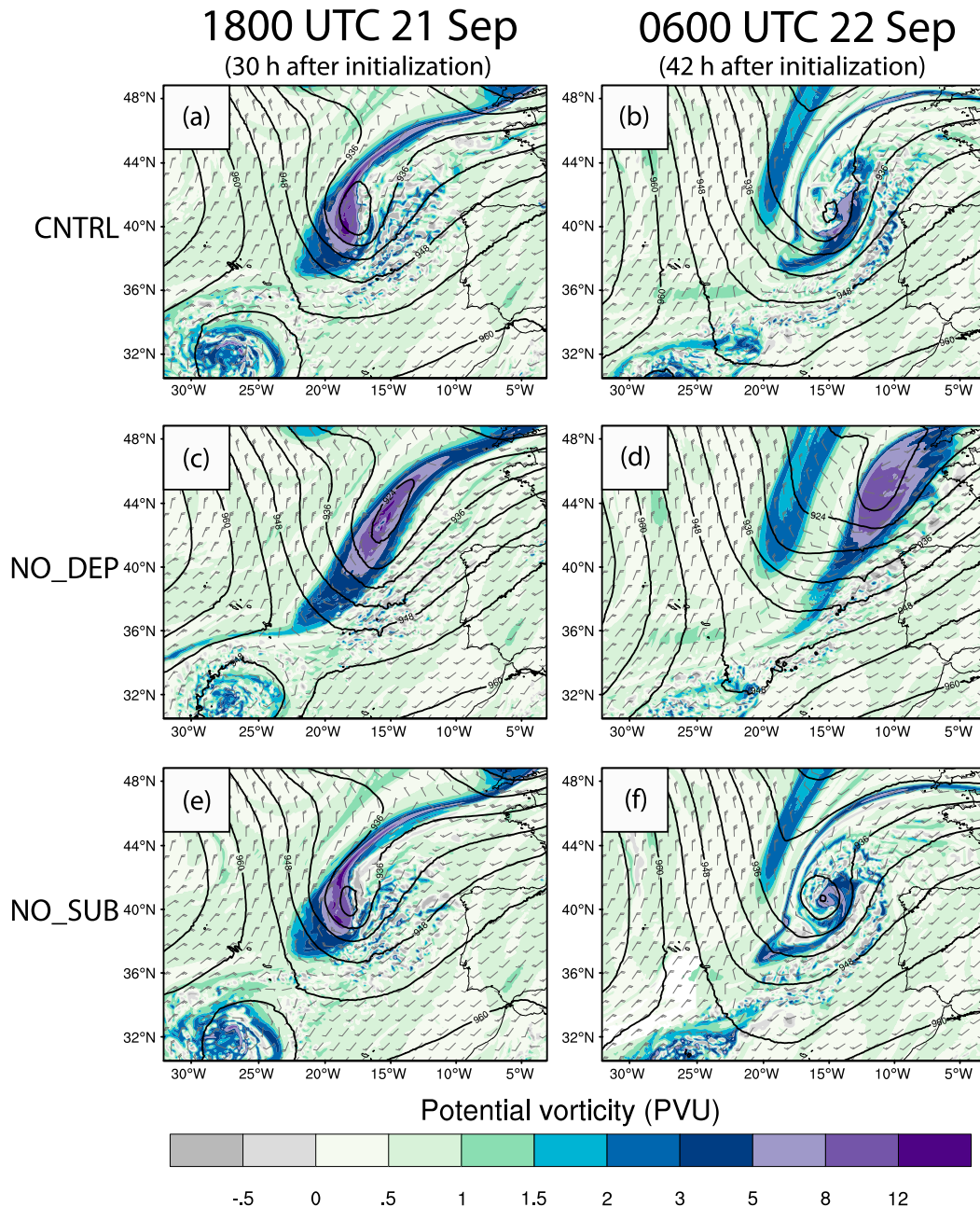
FIG. 11. Potential vorticity (shaded, PVU) and winds (half barb denotes 2.5, full barb denotes 5, pennant denotes 25 m s^{-1}), on the 320-K isentropic surface; 300-hPa geopotential height (black contours, dam). Comparison between (top) the control simulation (CNTRL), (middle) the simulation with no deposition heating (NO_DEP), and (bottom) the simulation with no sublimation cooling (NO_SUB) at (a),(c),(e) 1800 UTC 21 Sep and (b),(d),(f) 0600 UTC 22 Sep.

associated with an individual heating or cooling process, and D/Dt(PV) is the time rate of change of PV associated with that particular heating or cooling rate, following the flow. From Eq. (1), air parcels will experience an increase in PV below the level of maximum heating and conversely a decrease in PV above along ζ, for a positive vertical component of absolute vorticity. In general on the synoptic scale, the vertical component of absolute vorticity dominates, allowing the x and y components of the scalar product to be neglected, although strong vertical shear can tilt ζ appreciably into the horizontal, as shown in a case study by Lackmann (2002). In this case study however, the z component of the scalar product is approximately an order of
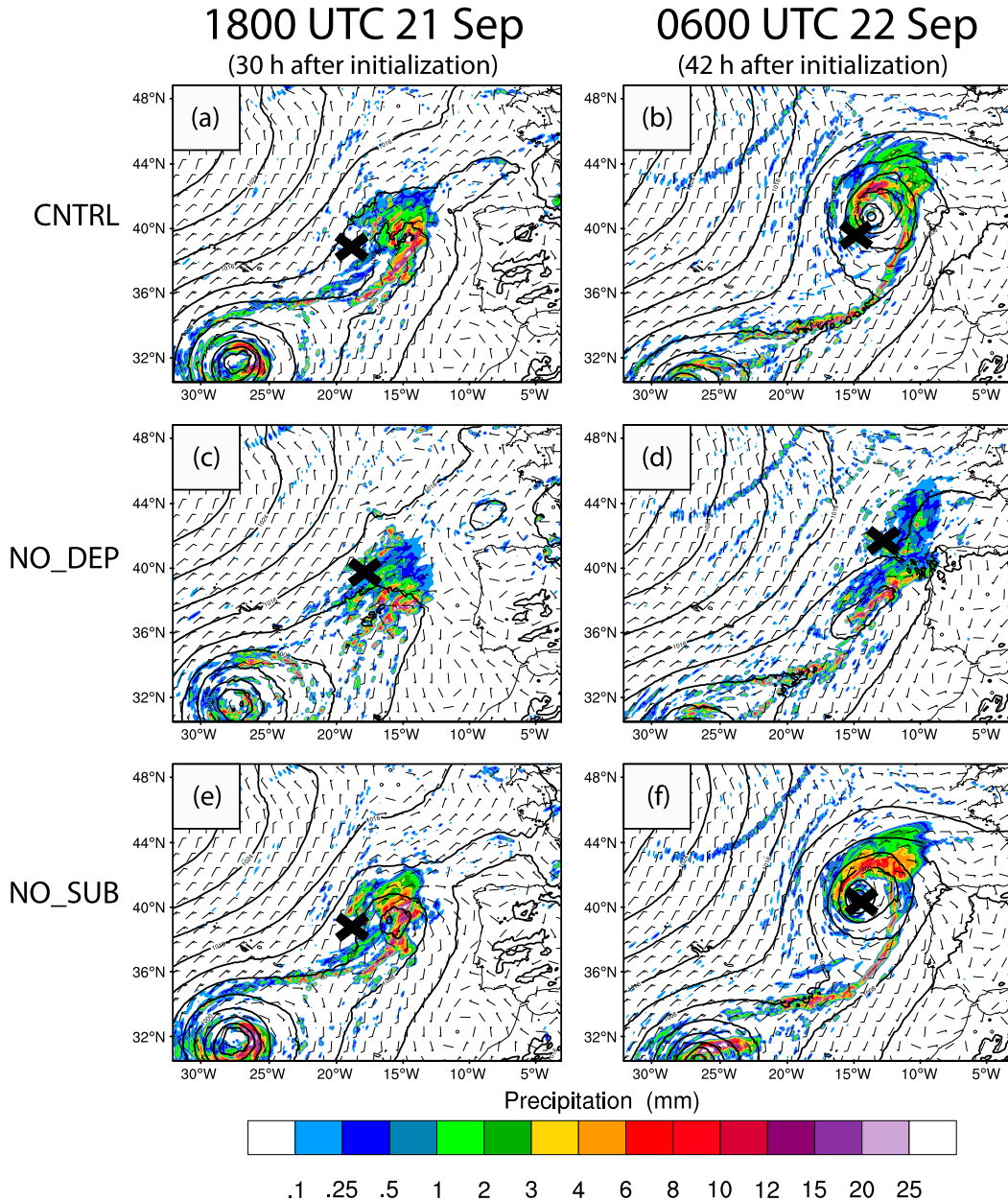
FIG. 12. Hourly accumulated precipitation (shaded, mm), 10-m winds (half barb denotes 2.5, full barb denotes 5, pennant denotes 25 m s^{-1}), and mean sea level pressure (black contours, hPa). Comparison between (top) the control simulation (CNTRL), (middle) the simulation with no deposition heating (NO_DEP), and (bottom) the simulation with no sublimation cooling (NO_SUB) at (a),(c),(e) 1800 UTC 21 Sep and (b),(d),(f) 0600 UTC 22 Sep. The black ×s mark the equatorward extent of the ≥ 5 PVU air associated with the PV streamer, and are determined manually from Fig. 11.

magnitude larger than the x and y components (not shown). From Eq. (1), instantaneous diabatic heating rates and PV tendencies attributable to individual microphysical processes are averaged over the cyclone and integrated along trajectories, using a similar method to Joos and Wernli (2012). In contrast to previous studies that concentrated on the warm conveyor belt (Joos and

Wernli 2012; Schemm et al. 2013; Martínez-Alvarado and Plant 2014; Schemm and Wernli 2014), the focus of these PV calculations is on the region close to the cyclone center.

The focus of this section is the modification of PV by microphysical heating and cooling. Thus, two main simplifying assumptions have been made. First, as
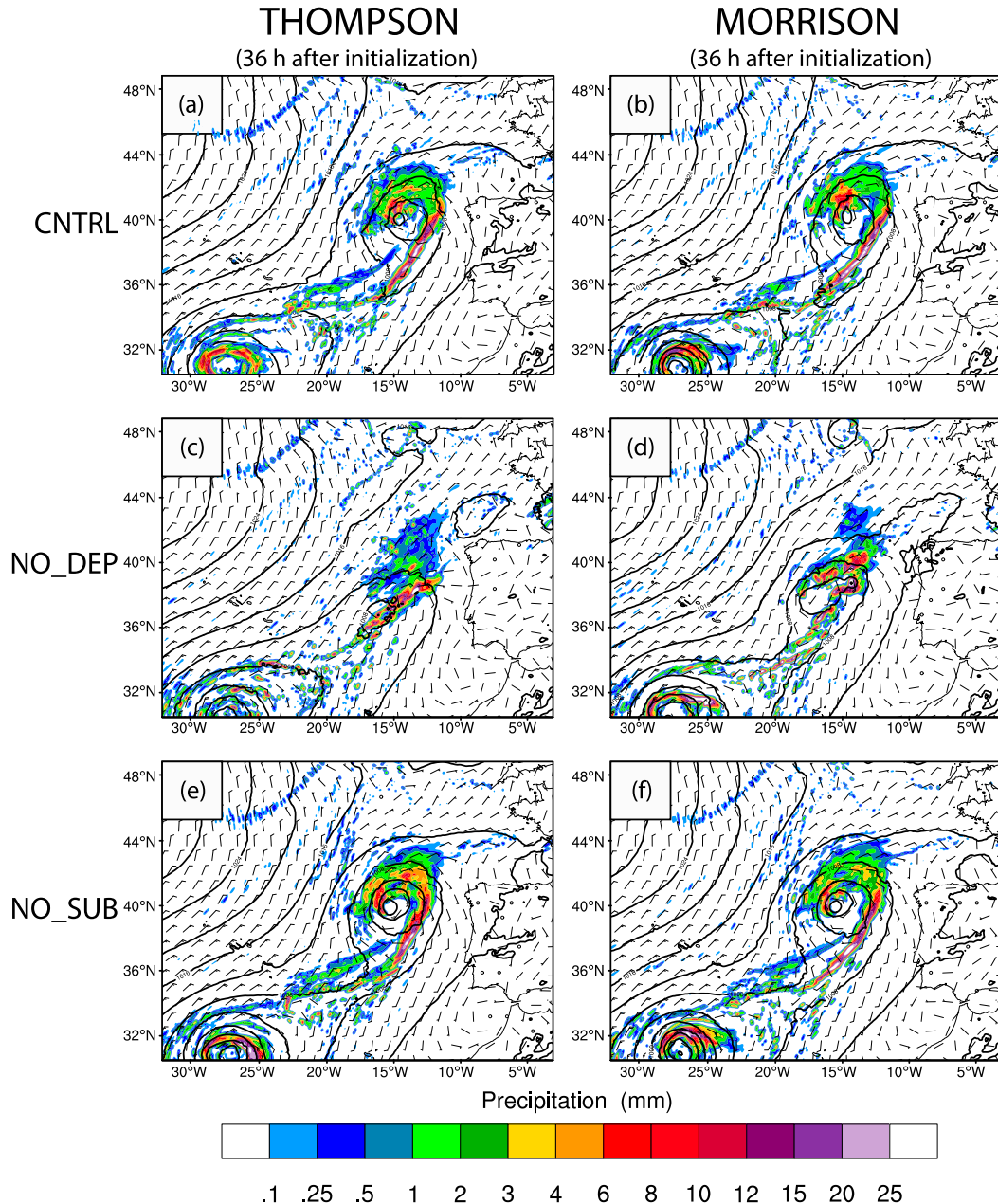
FIG. 13. Hourly accumulated precipitation (shaded, mm), 10-m winds (half barb denotes 2.5, full barb denotes 5, pennant denotes 25 m s^{-1}), and mean sea level pressure (black contours, hPa), valid at 0000 UTC 22 Sep. Comparison between (a),(c),(e) the Thompson and (b),(d),(f) Morrison double-moment microphysics parameterization schemes, for (top) the control simulation (CNTRL), (middle) the simulation with no deposition heating (NO_DEP), and (bottom) the simulation with no sublimation cooling (NO_SUB).

mentioned, the frictional generation of PV has been neglected in Eq. (1). Frictional generation of PV is proportional to the horizontal potential temperature (θ) gradient and can be nonnegligible within the boundary layer within the easterly flow north of the warm front (e.g., Stoelinga 1996). However, within this cyclone, this term is likely to contribute negligibly to total PV

tendencies relative to the diabatic term, given the relatively weak baroclinicity within the warm-frontal zone and the reduced magnitude of friction over the ocean surface relative to the land. Second, the PV tendencies attributable to radiative heating and cooling have been ignored. Previous studies have demonstrated that long-wave radiative cooling at the tropopause contributes to

WHOLE CYCLONE　　　　EAST OF PV STREAMER
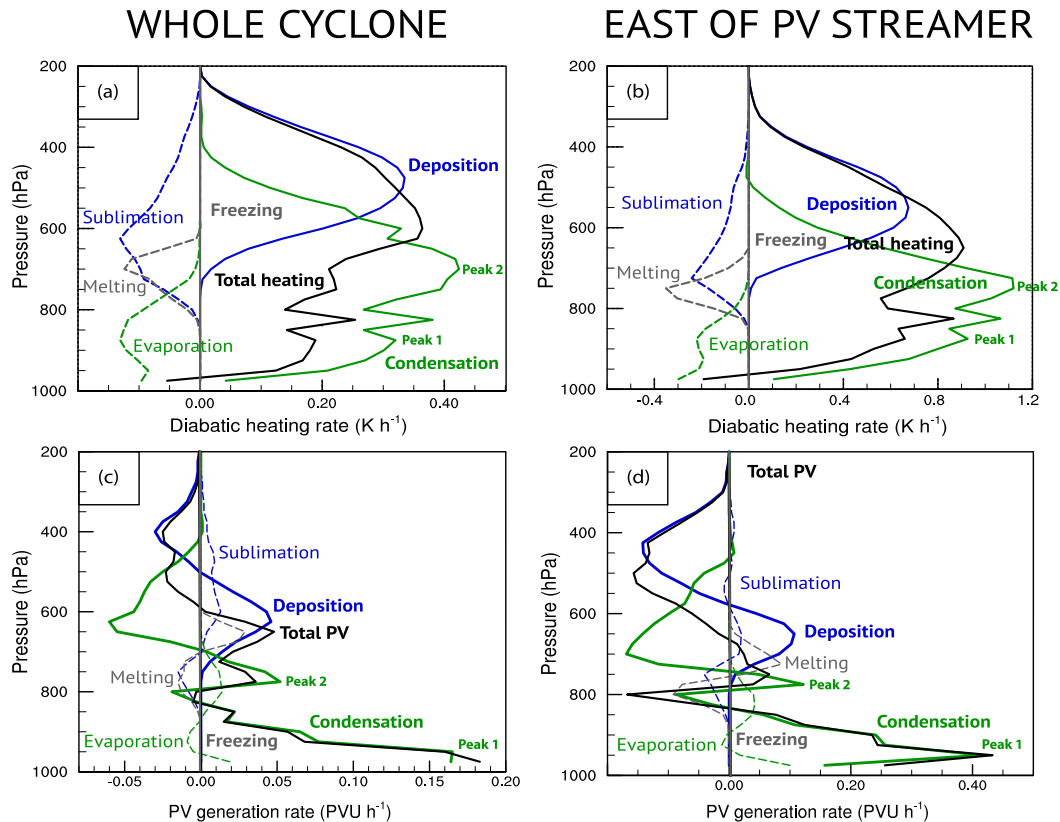
FIG. 14. (a)–(d) Vertical profile of area-averaged quantities from the control simulation (CNTRL) valid at 0000 UTC 22 Sep. Profiles (a) and (c) were calculated over the larger domain shown in Fig. 15, while profiles (b) and (d) were calculated over the smaller domain. In (a) and (b), diabatic heating and cooling rates $(K\,h^{-1})$ from microphysical processes are plotted, with heating terms in solid lines and cooling terms in dashed lines: condensation/ evaporation of cloud water and evaporation of rain (green), deposition and sublimation of snow and ice (blue), melting of snow/graupel and freezing of cloud/rainwater (gray), and total tendency (black). In (c) and (d), the corresponding diabatic PV generation rates $(PVU\,h^{-1})$ are plotted. The diabatic heating rates in (a) and (b), and the PV generation rates in (c) and (d) due to freezing are negligible. The two peaks in PV generation rate due to condensation heating in (c) and (d) are directly linked to the corresponding peaks in the condensation heating rate in (a) and (b), respectively.

positive PV generation in the lower stratosphere, thus enhancing the PV gradient across the tropopause (e.g., Chagnon et al. 2013; Martínez-Alvarado and Plant 2014). Chagnon et al. (2013) also discovered negative PV tendencies in the upper troposphere beneath the level of maximum radiative cooling in a cold-season North Atlantic cyclone, but found these negative PV tendencies to be smaller than those associated with microphysical heating. Because the main purpose of the present study is to quantify the contribution of deposition heating to changes in upper-tropospheric PV, the contribution of tropopause radiative cooling to changes in upper-tropospheric PV is not discussed further.

a. Diabatic heating rates

The distribution of diabatic heating and cooling within the developing cyclone at 0000 UTC 22 September is

illustrated by constructing area-averaged vertical profiles (Fig. 14). Two area averages are calculated. The first encompasses the entire cyclone and fracturing upper-level PV streamer (Fig. 15, larger box: 340 × 270 grid points). The second focuses on the region over and east of the fracturing PV streamer (Fig. 15, smaller box: 100 × 110 grid points). Area averages are first calculated over the entire cyclone (Fig. 14a) in order to compare results with previous studies that calculated microphysical heating and cooling rates on a similar spatial scale, along the entirety of the warm conveyor belt (e.g., Joos and Wernli 2012; Martínez-Alvarado et al. 2014). Area averaging over the smaller region east of the PV streamer (Fig. 14b) then allows quantification of the deposition heating rate within the key region east of the PV streamer versus over the entire cyclone. The results are not qualitatively sensitive to either the time chosen,
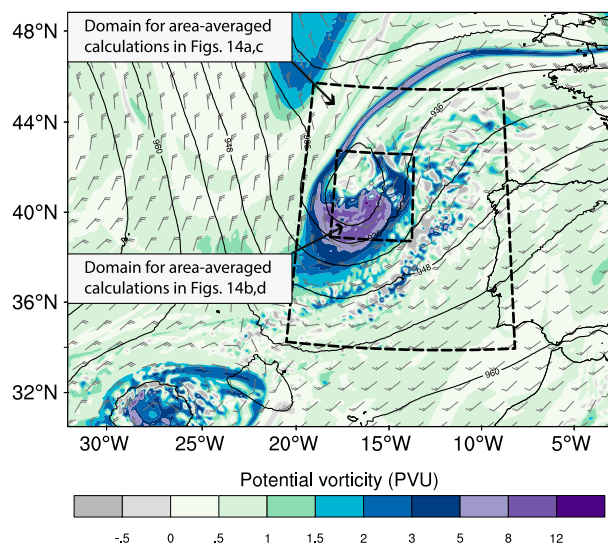
FIG. 15. Potential vorticity (shaded, PVU) and winds (half barb denotes 2.5, full barb denotes 5, pennant denotes 25 m s^{-1}), on the 320-K isentropic surface; 300-hPa geopotential height (black contours, dam), from the control simulation (CNTRL) at 0000 UTC 22 Sep. Overlaid (thick black dashed lines) are domain locations for the area-averaged vertical profiles in Fig. 14. The larger box (340 × 270 grid points) corresponds to the calculations in Figs. 14a and 14c, and the smaller box (100 × 110 grid points) corresponds to the calculations in Figs. 14b and 14d.

with similar profiles obtained at multiple times between 1500 UTC 21 September and 0300 UTC 22 September, or to the size of the smaller box[1] (not shown).

The total diabatic heating profile is dominated by condensation heating in the lower troposphere and deposition heating in the upper troposphere, both over the entire cyclone (Fig. 14a) and within the mesoscale region east of the PV streamer (Fig. 14b). Lower-tropospheric condensation heating is stronger than upper-tropospheric deposition heating, but not notably (Figs. 14a,b). Furthermore, the upper-tropospheric deposition heating maximum occurs at a level where contributions from all other processes are negligible, and thus accounts for almost all of the total heating at

---

[1] Averages were calculated over four additional boxes, two smaller (90 × 100 and 95 × 105 grid points) and two larger (105 × 115 and 110 × 120 grid points) than the original (100 × 110 grid points). Results for each of these boxes were qualitatively similar to the original, with negative PV tendencies due to deposition heating strongly impacting the total PV tendency. There was a dependence on box size, with the strongest negative PV tendencies obtained when averaging over the smallest box (90 × 100). Nevertheless, the conclusions drawn would be the same regardless of box size, with strong PV reduction due to deposition heating in the mesoscale region east of the PV streamer, but less so over the cyclone as a whole.

500 hPa and above (Figs. 14a,b). These results are qualitatively similar to those from previous case studies of both cold-season (Joos and Wernli 2012; Martínez-Alvarado et al. 2014) and warm-season (Dearden et al. 2016) eastern North Atlantic extratropical cyclones, suggesting that deposition heating may generally account for at least 75% of the upper-tropospheric diabatic heating, at the level of maximum deposition heating, within eastern North Atlantic cyclones.

Condensation heating rates in the lower troposphere exhibit multiple peaks between 900 and 700 hPa, with the two most prominent peaks labeled in Figs. 14a and 14b. The higher altitude peak ("Peak 2" in Figs. 14a,b) is collocated with the peak in cooling due to melting both on the cyclone scale (Fig. 14a; 700 hPa) and on the mesoscale (Fig. 14b; 750 hPa). As discussed by Woods et al. (2008) and also noted in a case study by Igel and van den Heever (2014), latent cooling by melting can increase the water supersaturation within the melting layer, thus indirectly contributing to an increase in condensation. A similar mechanism may be at work in this cyclone. Although the other cooling processes, sublimation and evaporation, contribute nonnegligibly to the total heating profile on both the cyclone scale (Fig. 14a) and on the mesoscale (Fig. 14b), the associated peaks in cooling rates are approximately half the size of the heating rate peaks associated with deposition and condensation. Accordingly, sublimation cooling is maximized between 750 and 500 hPa (along the cold front), but the total heating rate over this layer is still positive because of strong condensation and deposition heating (Figs. 14a,b). Similarly, evaporative cooling of rainfall at 750–950 hPa in the postcold-frontal air somewhat counteracts the positive tendency due to condensation heating (Figs. 14a,b). The freezing of cloud water and rainwater droplets also contributes to the total diabatic heating rate profile. However, the diabatic heating rates (and corresponding diabatic PV tendencies) associated with freezing are negligible in comparison to the other processes (Fig. 14) and are thus not discussed further.

b. Diabatic PV tendencies

The PV tendencies corresponding to the heating and cooling rates discussed in section 5a are shown in Fig. 14c across the entire cyclone and in Fig. 14d over the mesoscale region east of the PV streamer. Diabatic PV tendencies due to condensation are particularly strong in the lower troposphere where absolute vorticity is highest, both over the whole cyclone (Fig. 14c) and in the mesoscale region east of the PV streamer (Fig. 14d), with the two main peaks in the PV tendency profile directly related to the corresponding peaks in the heating rate profile (cf. Figs. 14b and 14d).

39 h after initialization
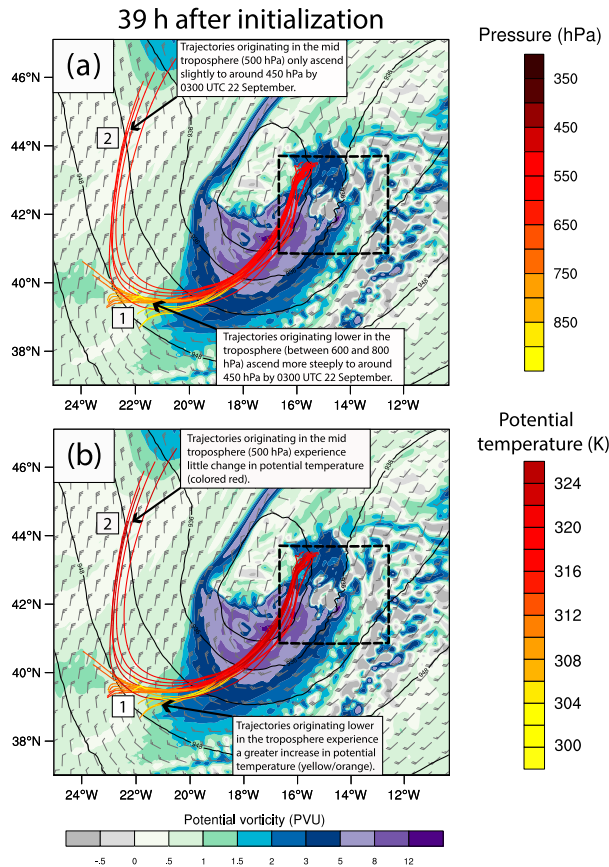
FIG. 16. Trajectories were released at every grid point within the black box at 500, 450, 400, and 350 hPa at 0300 UTC 22 Sep and run backward for 21 h. Selected trajectories that remained east of the PV streamer between 1500 UTC 21 Sep and 0300 UTC 22 Sep as the streamer fractured into a discrete anomaly were retained and are plotted in (a) with their pressure (hPa) and in (b) with their potential temperature (K) shaded. Overlaid is the potential vorticity (shaded, PVU) and winds (half barb denotes 2.5, full barb denotes 5, pennant denotes 25 m s^{-1}), on the 320-K isentropic surface and the 300-hPa geopotential height (black contours, dam), valid at 0300 UTC 22 Sep.

Averaged over the entire cyclone, the negative PV tendencies due to deposition heating above the heating maximum are less extensive[2] than the positive tendencies below the maximum (Fig. 14c), indicative of decreasing absolute vorticity with heights above the 450-hPa heating maximum (Fig. 14a). This result is similar to previous case studies in which PV tendencies attributed to condensation heating dominated PV tendencies

attributed to other microphysical processes along warm conveyor belt trajectories (Joos and Wernli 2012; Martínez-Alvarado et al. 2014). Conversely, on the mesoscale, the negative upper-tropospheric PV tendencies attributed to deposition heating are more extensive relative both to the positive PV tendencies below the heating maximum and to the PV tendencies associated with the other microphysical processes (Fig. 14d). This reduction in PV due to deposition heating at the level of the PV streamer (500–350 hPa), in conjunction with the enhanced divergent outflow discussed in sections 3 and 4, likely contributed to the slower eastward movement of the PV streamer and to its eventual fracture.

The PV tendencies associated with sublimation, evaporation, and melting are generally smaller than those associated with condensation and deposition (Figs. 14c,d). However, between 700 and 625 hPa, positive PV tendencies above the 700-hPa peak in cooling due to melting (cf. Figs. 14a and 14c) contribute to the positive total PV tendency and help to offset the negative tendencies above the condensation heating maximum (Fig. 14c). This effect is also apparent over the mesoscale region east of the PV streamer between 650 and 750 hPa (Fig. 14d).

c. Trajectories

Martínez-Alvarado et al. (2016) show how the integration of heating and cooling rates along trajectories (tracers in their case) indicates the physical processes that are contributing most to cross-isentropic motion of air parcels and thus bringing the air parcels to their current θ. To complement the instantaneous heating profiles and tendencies in the previous sections we now present integrated heating and PV modification along trajectories in CNTRL, to identify the most important physical processes changing θ and PV in an air parcel.

Trajectory positions were calculated offline at 10-min intervals using the WRF software Read/Interpolate/Plot (RIP4; Stoelinga 2009), and the model grid points closest to the trajectory positions were chosen. Atmospheric variables (θ, PV, heating/cooling rates, and corresponding PV tendencies) were calculated at these model grid points every 10 min as the PV streamer fractured into a discrete anomaly between 1500 UTC 21 September and 0300 UTC 22 September, allowing for the calculation of integrated totals along trajectories. Trajectories were released on four upper-tropospheric pressure levels (500, 450, 400, and 350 hPa) at every grid point within the box shown (Fig. 16) at 0300 UTC 22 September, during the cyclone's development phase, and run backward for 21 h. Trajectories that remained to the east of the PV streamer as the streamer fractured into a discrete anomaly at 320 K

---

[2] Calculating the area under the curve reveals that over the whole cyclone, the negative PV tendency due to deposition heating is about 60% of the positive PV tendency (Fig. 14c), whereas on the mesoscale, the negative PV tendency equates to over 200% of the positive PV tendency (Fig. 14d).
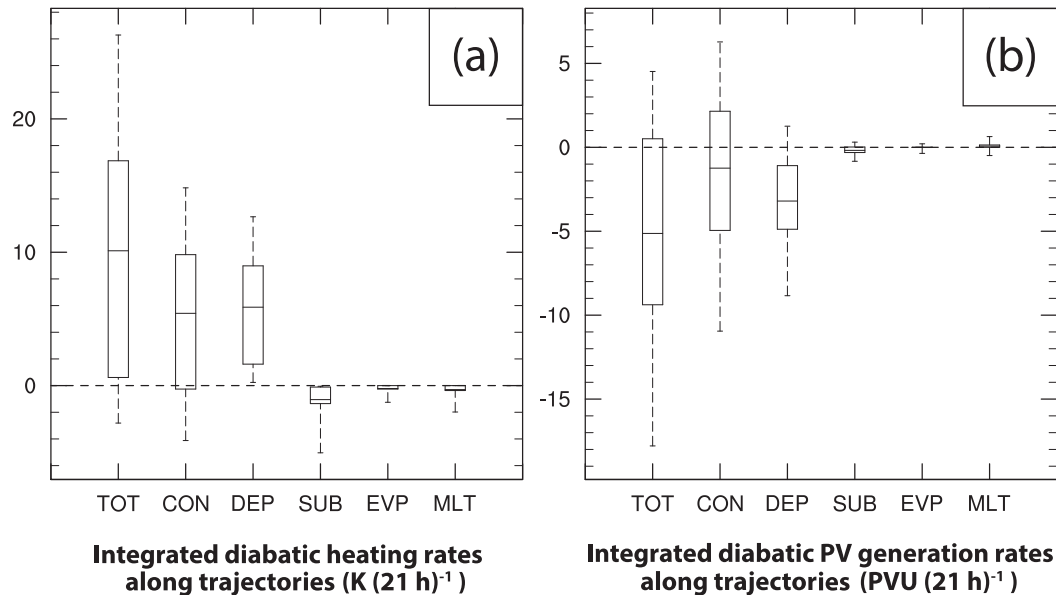
FIG. 17. (a) Integrated mean diabatic heating rates $[K (21 h)^{-1}]$ along trajectories between 0600 UTC 21 Sep and 0300 UTC 22 Sep. Plotted are contributions from total microphysical heating (TOT), condensation/evaporation of cloud water (CON), depositional growth of snow and ice (DEP), sublimation of snow and ice (SUB), evaporation of rain (EVP), and melting of snow and graupel (MLT). (b) Integrated mean diabatic PV generation rates $[PVU (21 h)^{-1}]$ corresponding to the mean diabatic heating rates in (a). The box shows the 25%–75% range and the whiskers indicate the 5%–95% percentiles.

between 1500 UTC 21 September and 0300 UTC 22 September are analyzed further (Fig. 16), and can be separated into two main groups. The first group (labeled 1 in Fig. 16) originated near the incipient cyclone in the low to midtroposphere between 600 and 800 hPa (Fig. 16a). These trajectories ascended as they moved northeast, experiencing increases in θ of between 10 and 20 K (Fig. 16b). The second group (labeled 2 in Fig. 16) originated northwest of the incipient cyclone in the midtroposphere around 500 hPa and moved south before turning cyclonically north near 23°W (Fig. 16a), and experienced smaller changes in θ during the 21 h (Fig. 16b).

Deposition and condensation heating dominate the integrated mean diabatic heating rates along the selected trajectories, each contributing about 5 K to the total diabatic heating in the 21 h between 0600 UTC 21 September and 0300 UTC 22 September (Fig. 17a) and thus contributing most strongly to cross-isentropic motion of air parcels (Martínez-Alvarado et al. 2016). The contributions from cooling due to sublimation, evaporation, and melting are negligible in comparison (Fig. 17a). These integrated mean heating and cooling rates are qualitatively similar to those in previous warm conveyor belt studies (e.g., Joos and Wernli 2012; Martínez-Alvarado and Plant 2014), although variability among individual trajectories in this study is much greater, as illustrated by the large range in

5%–95% values in Fig. 17a relative to those in Fig. 5 in Joos and Wernli (2012). The corresponding integrated PV tendencies (Fig. 17b) reveal a negative total PV tendency over the 21 h (mean value of −5.1 PVU) with deposition heating contributing most strongly (−3.2 PVU). Condensation heating also contributes to the direct diabatic reduction in PV in the region east of the upper-tropospheric PV anomaly (−1.2 PVU), but to a lesser extent. As with the diabatic heating and cooling rates, the contributions of sublimation, evaporation, and melting to changes in PV along trajectories are about an order of magnitude smaller than those associated with deposition and condensation heating (Fig. 17b). Equating smaller integrated PV tendencies with lesser impacts upon extratropical cyclone track and intensity, these results support previous studies in which microphysical cooling impacted negligibly upon cyclone track and intensity (e.g., Parker and Thorpe 1995; Clough et al. 2000; Forbes and Clark 2003).

To conclude, deposition heating is the strongest contributor to negative PV tendencies along selected trajectories that remained east of the PV streamer between 1500 UTC 21 September and 0300 UTC 22 September (Fig. 17b), supporting the results from the sensitivity simulations in section 4 and the area-averaged calculations earlier in this section. This result suggests that deposition heating may reduce upper-level PV near the

center of extratropical cyclones where midtropospheric absolute vorticity is large, more strongly than it reduces upper-level PV along the warm conveyor belt where midtropospheric absolute vorticity is generally small (e.g., Joos and Wernli 2012; Martínez-Alvarado et al. 2014). The wider implication is that upper-level PV modification by deposition heating must be accounted for, in addition to PV modification by condensation heating, to fully understand the dynamical impact of latent heat release on the synoptic-scale development of extratropical cyclones. Indeed, the results here, in conjunction with the synoptic-scale response of this cyclone, show that the collocation of deposition heating and positive absolute vorticity in the upper troposphere can lead to substantial PV modification and a very different cyclone evolution to that when deposition heating is suppressed. However, the strength of PV modification by deposition heating is likely sensitive to factors such as the freezing level. We hypothesize that in cold-season cyclones with a lower freezing level and a deposition heating maximum consequently closer to the surface, upper-tropospheric PV reduction due to deposition heating may actually be less pronounced than in the cyclone studied here, given the less favorable collocation of the deposition heating maximum with the enhanced vorticity of the upper-tropospheric PV anomaly.

6. Conclusions

This study used convection-permitting WRF simulations, area-averaged calculations of diabatic heating rates and PV tendencies, and integrated trajectory calculations of diabatic heating rates and PV tendencies to demonstrate the dynamical response of an eastern North Atlantic cyclone to the removal of deposition heating, with the cyclone's track and intensity substantially altered when deposition heating was removed. In the control simulation (CNTRL), a surface cyclone formed immediately east of an upper-tropospheric PV streamer as it thinned and fractured into a discrete PV anomaly between 1500 UTC 21 September and 0300 UTC 22 September. When deposition heating was suppressed (NO_DEP), the PV streamer moved northeastward more quickly and the surface cyclone was 18 hPa shallower in its mature phase than in CNTRL.

Area-averaged calculations of instantaneous diabatic heating and cooling rates during the cyclone's development phase at 0000 UTC 22 September revealed that condensation and deposition heating dominated the total heating profile, both over the entire cyclone and within a smaller region east of the PV streamer. Condensation heating generated strong positive PV in the

lower troposphere, in agreement with previous case studies. In the upper troposphere, negative PV tendencies due to deposition heating contributed most strongly to the total PV tendency. These negative PV tendencies were particularly pronounced in the mesoscale region east of the PV streamer. Integrated calculations along selected backward trajectories, which remained to the east of the PV streamer as it fractured into a discrete anomaly between 1500 UTC 21 September and 0300 UTC 22 September, revealed that deposition heating contributed more strongly than other microphysical processes to negative PV tendencies, supporting earlier sensitivity simulations and area-averaged calculations.

The strong synoptic-scale response of this cyclone contrasts with the much weaker response found by Dearden et al. (2016) in a similar study of two summer cyclones over the United Kingdom, showing that the collocation of deposition heating with positive absolute vorticity in the upper troposphere can lead to substantial PV modification and a very different cyclone evolution to that when deposition heating is suppressed. This points to the need for an accurate representation of ice processes for synoptic-scale weather forecasting; despite the similarity between the simulations with the Thompson and Morrison schemes in this case there are known deficiencies with current parameterization schemes, for example, regarding particle shape (Dearden et al. 2016). Further work is needed to determine what effect the uncertainty in deposition heating parameterization introduces to the evolution of cyclones such as that studied here.

REFERENCES

Ahmadi-Givi, F., G. C. Craig, and R. S. Plant, 2004: The dynamics of a midlatitude cyclone with very strong latent heat release. *Quart. J. Roy. Meteor. Soc.*, **130**, 295–323, doi:10.1256/qj.02.226.

Anthes, R. A., Y.-H. Kuo, and J. R. Gyakum, 1983: Numerical simulations of a case of explosive marine cyclogenesis. *Mon. Wea. Rev.*, **111**, 1174–1188, doi:10.1175/1520-0493(1983)111<1174:NSOACO>2.0.CO;2.

Bosart, L. F., and G. M. Lackmann, 1995: Postlandfall tropical cyclone reintensification in a weakly baroclinic environment: A case study of Hurricane David (September 1979). *Mon. Wea. Rev.*, **123**, 3268–3291, doi:10.1175/1520-0493(1995)123<3268:PTCRIA>2.0.CO;2.

Brennan, M. J., G. M. Lackmann, and K. M. Mahoney, 2008: Potential vorticity (PV) thinking in operations: The utility of nonconservation. *Wea. Forecasting*, **23**, 168–182, doi:10.1175/2007WAF2006044.1.

Carlson, T. N., 1980: Airflow through midlatitude cyclones and the comma cloud pattern. *Mon. Wea. Rev.*, **108**, 1498–1509, doi:10.1175/1520-0493(1980)108<1498:ATMCAT>2.0.CO;2.

Chagnon, J., S. Gray, and J. Methven, 2013: Diabatic processes modifying potential vorticity in a North Atlantic cyclone. *Quart. J. Roy. Meteor. Soc.*, **139**, 1270–1282, doi:10.1002/qj.2037.

Chen, S.-J., and L. Dell'Osso, 1987: A numerical case study of east Asian coastal cyclogenesis. *Mon. Wea. Rev.*, **115**, 477–487, doi:10.1175/1520-0493(1987)115<0477:ANCSOE>2.0.CO;2.

Clough, S. A., and R. A. A. Franks, 1991: The evaporation of frontal and other stratiform precipitation. *Quart. J. Roy. Meteor. Soc.*, **117**, 1057–1080, doi:10.1002/qj.49711750109.

——, H. W. Lean, N. M. Roberts, and R. M. Forbes, 2000: Dynamical effects of ice sublimation in a frontal wave. *Quart. J. Roy. Meteor. Soc.*, **126**, 2405–2434, doi:10.1002/qj.49712656804.

Danard, M. B., and G. E. Ellenton, 1980: Physical influences on east coast cyclogenesis. *Atmos.–Ocean*, **18**, 65–82, doi:10.1080/07055900.1980.9649078.

Davis, C. A., 1992: A potential-vorticity diagnosis of the importance of initial structure and condensational heating in observed extratropical cyclogenesis. *Mon. Wea. Rev.*, **120**, 2409–2428, doi:10.1175/1520-0493(1992)120<2409:APVDOT>2.0.CO;2.

——, M. T. Stoelinga, and Y.-H. Kuo, 1993: The integrated effect of condensation in numerical simulations of extratropical cyclogenesis. *Mon. Wea. Rev.*, **121**, 2309–2330, doi:10.1175/1520-0493(1993)121<2309:TIEOCI>2.0.CO;2.

Dearden, C., P. J. Connolly, G. Lloyd, J. Crosier, K. N. Bower, T. W. Choularton, and G. Vaughan, 2014: Diabatic heating and cooling rates derived from in situ microphysics measurements: A case study of a wintertime U.K. cold front. *Mon. Wea. Rev.*, **142**, 3100–3125, doi:10.1175/MWR-D-14-00048.1.

——, G. Vaughan, T. Tsai, and J.-P. Chen, 2016: Exploring the diabatic role of ice microphysical processes in two North Atlantic summer cyclones. *Mon. Wea. Rev.*, **144**, 1249–1272, doi:10.1175/MWR-D-15-0253.1.

Dickinson, M. J., L. F. Bosart, W. E. Bracken, G. J. Hakim, D. M. Schultz, M. A. Bedrick, and K. R. Tyle, 1997: The March 1993 superstorm cyclogenesis: Incipient phase synoptic- and convective-scale flow interaction and model performance. *Mon. Wea. Rev.*, **125**, 3041–3072, doi:10.1175/1520-0493(1997)125<3041:TMSCIP>2.0.CO;2.

Forbes, R. M., and P. A. Clark, 2003: Sensitivity of extratropical cyclone mesoscale structure to the parametrization of ice microphysical processes. *Quart. J. Roy. Meteor. Soc.*, **129**, 1123–1148, doi:10.1256/qj.01.171.

——, and R. J. Hogan, 2006: Observations of the depth of ice particle evaporation beneath frontal cloud to improve NWP modelling. *Quart. J. Roy. Meteor. Soc.*, **132**, 865–883, doi:10.1256/qj.04.187.

Grams, C. M., and Coauthors, 2011: The key role of diabatic processes in modifying the upper-tropospheric wave guide: A North Atlantic case study. *Quart. J. Roy. Meteor. Soc.*, **137**, 2174–2193, doi:10.1002/qj.891.

Hong, S.-Y., Y. Noh, and J. Dudhia, 2006: A new vertical diffusion package with an explicit treatment of entrainment processes. *Mon. Wea. Rev.*, **134**, 2318–2341, doi:10.1175/MWR3199.1.

Hoskins, B. J., M. E. McIntyre, and A. W. Robertson, 1985: On the use and significance of isentropic potential vorticity maps. *Quart. J. Roy. Meteor. Soc.*, **111**, 877–946, doi:10.1002/qj.49711147002.

Huang, H.-C., and K. A. Emanuel, 1991: The effects of evaporation on frontal circulations. *J. Atmos. Sci.*, **48**, 619–628, doi:10.1175/1520-0469(1991)048<0619:TEOEOF>2.0.CO;2.

Iacono, M. J., J. S. Delamere, E. J. Mlawer, M. W. Shephard, S. A. Clough, and W. D. Collins, 2008: Radiative forcing by long-lived greenhouse gases: Calculations with the AER radiative transfer models. *J. Geophys. Res.*, **113**, D13103, doi:10.1029/2008JD009944.

Igel, A. L., and S. C. van den Heever, 2014: The role of latent heating in warm frontogenesis. *Quart. J. Roy. Meteor. Soc.*, **140**, 139–150, doi:10.1002/qj.2118.

Joos, H., and H. Wernli, 2012: Influence of microphysical processes on the potential vorticity development in a warm conveyor belt: A case-study with the limited-area model COSMO. *Quart. J. Roy. Meteor. Soc.*, **138**, 407–418, doi:10.1002/qj.934.

Kain, J. S., and J. M. Fritsch, 1990: A one-dimensional entraining/detraining plume model and its application in convective parameterization. *J. Atmos. Sci.*, **47**, 2784–2802, doi:10.1175/1520-0469(1990)047<2784:AODEPM>2.0.CO;2.

Kuo, Y.-H., and R. J. Reed, 1988: Numerical simulation of an explosively deepening cyclone in the eastern Pacific. *Mon. Wea. Rev.*, **116**, 2081–2105, doi:10.1175/1520-0493(1988)116<2081:NSOAED>2.0.CO;2.

Lackmann, G. M., 2002: Cold-frontal potential vorticity maxima, the low-level jet, and moisture transport in extratropical cyclones. *Mon. Wea. Rev.*, **130**, 59–74, doi:10.1175/1520-0493(2002)130<0059:CFPVMT>2.0.CO;2.

Martínez-Alvarado, O., and R. S. Plant, 2014: Parametrized diabatic processes in numerical simulations of an extratropical cyclone. *Quart. J. Roy. Meteor. Soc.*, **140**, 1742–1755, doi:10.1002/qj.2254.

——, H. Joos, J. Chagnon, M. Boettcher, S. L. Gray, R. S. Plant, J. Methven, and H. Wernli, 2014: The dichotomous structure of the warm conveyor belt. *Quart. J. Roy. Meteor. Soc.*, **140**, 1809–1824, doi:10.1002/qj.2276.

——, S. L. Gray, and J. Methven, 2016: Diabatic processes and the evolution of two contrasting summer extratropical cyclones. *Mon. Wea. Rev.*, **144**, 3251–3276, doi:10.1175/MWR-D-15-0395.1.

Martius, O., C. Schwierz, and H. C. Davies, 2007: Breaking waves at the tropopause in the wintertime Northern Hemisphere: Climatological analyses of the orientation and the theoretical LC1/2 classification. *J. Atmos. Sci.*, **64**, 2576–2592, doi:10.1175/JAS3977.1.

——, ——, and M. Sprenger, 2008: Dynamical tropopause variability and potential vorticity streamers in the Northern

Hemisphere—A climatological analysis. *Adv. Atmos. Sci.*, **25**, 367–379, doi:10.1007/s00376-008-0367-z.

Met Office, 2012: Storm caused by most intense low to cross UK in September in 30 years. Posted 26 September 2012, Met Office Press Office. [Available online at http://metofficenews. wordpress.com/2012/09/26/storm-caused-by-most-intense-low-to-cross-uk-in-30-years/.]

Milbrandt, J. A., and H. Morrison, 2013: Prediction of graupel density in a bulk microphysics scheme. *J. Atmos. Sci.*, **70**, 410–429, doi:10.1175/JAS-D-12-0204.1.

Monin, A. S., and A. M. Obukhov, 1954: Basic laws of turbulent mixing in the surface layer of the atmosphere. *Tr. Geofiz. Inst., Akad. Nauk SSSR*, **24**, 163–187.

Morrison, H., J. A. Curry, and V. I. Khvorostyanov, 2005: A new double-moment microphysics parameterization for application in cloud and climate models. Part I: Description. *J. Atmos. Sci.*, **62**, 1665–1677, doi:10.1175/JAS3446.1.

Munsell, E. B., J. A. Sippel, S. A. Braun, Y. Weng, and F. Zhang, 2015: Dynamics and predictability of Hurricane Nadine (2012) evaluated through convection-permitting ensemble analysis and forecasts. *Mon. Wea. Rev.*, **143**, 4514–4532, doi:10.1175/MWR-D-14-00358.1.

Pantillon, F. P., J.-P. Chaboureau, and E. Richard, 2016: Vortex–vortex interaction between Hurricane Nadine (2012) and an Atlantic cutoff dropping the predictability over the Mediterranean. *Quart. J. Roy. Meteor. Soc.*, **142**, 419–432, doi:10.1002/qj.2635.

Parker, D. J., and A. J. Thorpe, 1995: The role of snow sublimation in frontogenesis. *Quart. J. Roy. Meteor. Soc.*, **121**, 763–782, doi:10.1002/qj.49712152403.

Parry, S., T. Marsh, and M. Kendon, 2013: 2012: From drought to floods in England and Wales. *Weather*, **68**, 268–273, doi:10.1002/wea.2152.

Plant, R. S., G. C. Craig, and S. L. Gray, 2003: On a threefold classification of extratropical cyclogenesis. *Quart. J. Roy. Meteor. Soc.*, **129**, 2989–3012, doi:10.1256/qj.02.174.

Posselt, D. J., and J. E. Martin, 2004: The effect of latent heat release on the evolution of a warm occluded thermal structure. *Mon. Wea. Rev.*, **132**, 578–599, doi:10.1175/1520-0493(2004)132<0578:TEOLHR>2.0.CO;2.

Raymond, D. J., 1992: Nonlinear balance and potential-vorticity thinking at large Rossby number. *Quart. J. Roy. Meteor. Soc.*, **118**, 987–1015, doi:10.1002/qj.49711850708.

Reed, R. J., G. A. Grell, and Y.-H. Kuo, 1993a: The ERICA IOP 5 storm. Part I: Analysis and simulation. *Mon. Wea. Rev.*, **121**, 1577–1594, doi:10.1175/1520-0493(1993)121<1577:TEISPI>2.0.CO;2.

——, ——, and ——, 1993b: The ERICA IOP 5 storm. Part II: Sensitivity tests and further diagnosis based on model output. *Mon. Wea. Rev.*, **121**, 1595–1612, doi:10.1175/1520-0493(1993)121<1595:TEISPI>2.0.CO;2.

——, Y.-H. Kuo, and S. Low-Nam, 1994: An adiabatic simulation of the ERICA IOP 4 storm: An example of quasi-ideal frontal cyclone development. *Mon. Wea. Rev.*, **122**, 2688–2708, doi:10.1175/1520-0493(1994)122<2688:AASOTE>2.0.CO;2.

Rossa, A. M., H. Wernli, and H. C. Davies, 2000: Growth and decay of an extra-tropical cyclone's PV-tower. *Meteor. Atmos. Phys.*, **73**, 139–156, doi:10.1007/s007030050070.

Schemm, S., and H. Wernli, 2014: The linkage between the warm and the cold conveyor belts in an idealized extratropical cyclone. *J. Atmos. Sci.*, **71**, 1443–1459, doi:10.1175/JAS-D-13-0177.1.

——, ——, and L. Papritz, 2013: Warm conveyor belts in idealized moist baroclinic wave simulations. *J. Atmos. Sci.*, **70**, 627–652, doi:10.1175/JAS-D-12-0147.1.

Schumacher, R. S., T. J. Galarneau, and L. F. Bosart, 2011: Distant effects of a recurving tropical cyclone on rainfall in a midlatitude convective system: A high-impact predecessor rain event. *Mon. Wea. Rev.*, **139**, 650–667, doi:10.1175/2010MWR3453.1.

Skamarock, W. C., and Coauthors, 2008: A description of the Advanced Research WRF version 3. NCAR Tech. Note NCAR/TN-475+STR, 113 pp., doi:10.5065/D68S4MVH.

Stoelinga, M. T., 1996: A potential vorticity-based study of the role of diabatic heating and friction in a numerically simulated baroclinic cyclone. *Mon. Wea. Rev.*, **124**, 849–874, doi:10.1175/1520-0493(1996)124<0849:APVBSO>2.0.CO;2.

——, 2009: A users' guide to RIP version 4.5: A program for visualizing mesoscale model output. Accessed 16 February 2016. [Available online at http://www2.mmm.ucar.edu/wrf/users/docs/ripug.htm.]

Szeto, K. K., and R. E. Stewart, 1997: Effects of melting on frontogenesis. *J. Atmos. Sci.*, **54**, 689–702, doi:10.1175/1520-0469(1997)054<0689:EOMOF>2.0.CO;2.

Thompson, G., P. R. Field, R. M. Rasmussen, and W. D. Hall, 2008: Explicit forecasts of winter precipitation using an improved bulk microphysics scheme. Part II: Implementation of a new snow parameterization. *Mon. Wea. Rev.*, **136**, 5095–5115, doi:10.1175/2008MWR2387.1.

Woods, C. P., J. D. Locatelli, and M. T. Stoelinga, 2008: The IMPROVE-1 storm of 1–2 February 2001. Part IV: Precipitation enhancement across the melting layer. *J. Atmos. Sci.*, **65**, 1087–1092, doi:10.1175/2007JAS2247.1.